Chemical Engineering Science 292 (2024) 120005

Contents lists available at ScienceDirect

Chemical Engineering Science

journal homepage: www.elsevier.com/locate/ces

Pore structure-transport relationships in high-temperature shift catalyst pellets studied by integrated multiscale porosimetry and X-ray tomography

Suleiman Mousa [a,b], Toby Beech [c], Emma Softley [c], Robin S. Fletcher [c], Gordon Kelly [c], Emily Viney [c], Sean P. Rigby [a,*]

[a] Department of Chemical and Environmental Engineering, Faculty of Engineering, University of Nottingham, University Park, Nottingham, NG7 2RD, UK
[b] Department of Chemical Engineering, King Faisal University, Eastern Province – AlAhsa, P.O. Box 400, 31982, Saudi Arabia
[c] Johnson Matthey, P.O. Box 1, Belasis Avenue, Billingham, Cleveland TS23 1LB, UK

ARTICLE INFO

Keywords:
X-ray computed tomography
Neural network
Adsorption
Porosity
Diffusion

ABSTRACT

Diffusion-limited, heterogeneously-catalysed processes mean choices influencing pore structure-transport relationships, made during pellet fabrication, affect product performance. This work shows how the 'sifting strategy' can identify the critical aspects of a highly complex catalyst pellet pore structure that control mass transport to construct an idiosyncratic, minimalist model. This is implemented using fully-integrated gas over-condensation, mercury porosimetry and X-ray tomography experiments. It showed high temperature shift (HTS) catalyst pellets had a trimodal pore structure. The second mode, consisting of macropores within the roll-compacted feed particles, controlled mass transport. Knudsen-regime mass transport was shown to be critically-controlled by an incipiently-percolating cluster of these intermediate-sized macropores, as its rate could be drastically reduced via introduction of very few blockages via mercury entrapment. This incipiently percolating network could be represented by a lattice-based, random cluster model. X-ray tomographic images, analysed with an AI segmentation algorithm, validated the proposed model of interpretation for the indirect characterization data.

1. Introduction

For many heterogeneously-catalysed processes, the rate-limiting step is mass transport to the catalytically active site (Twigg, 2014). The high temperature shift (HTS) reaction, over iron-chromia catalyst pellets, is an example of such a reaction. The effectiveness factor for typical commercial HTS catalysts varies from ~ 99 % at 310 °C to only 24 % at 450 °C (Twigg, 2014). The rate of mass transport in the catalyst pellets is determined by the nature of the pore structure. It is not possible to use the catalyst in powder form, to reduce the particle size, in a full-scale reactor because of the increased pressure drop, and, thus, the catalyst is typically used in pelletised form. Heterogeneous catalyst pellets are complex hierarchical structures, with features affecting mass transport arising over several length-scales due to the properties of the raw materials and engineering choices made for the processing route during their fabrication.

The compaction process to form tablets can lead to structural heterogeneity on the length-scale of the pellet itself (Jacobsen et al. (2014); Rigby et al.,1996; Dudhat et al., 2017; Elsergany et al., 2020). While the raw material for heterogeneous catalysts often comes in the form of fine powder, this is generally not used to form the compact. This is because of powder-handling issues (Dudhat et al., 2017). To avoid these problems the feed for the tabletting step is often pre-compacted to larger particle sizes. Roll-compaction and spray-drying are methods often used to produce larger feed particles from raw powder. However, these processes mean that the pellet feed itself is a hierarchical structure. Computerised X-ray tomography (CXT) has shown that individual roll-compacted or spray-dried feed particles are, themselves, composite structures, consisting of still smaller scale fragments that are still larger than the original powder (Mousa et al., 2023a,b). Indeed, the composite nature of the pellet feed often means that, overall, the pellet has a fractal-like structure (Mousa et al., 2023a,b). Further, several studies indicate that the occurrence of large, internal, macroporous voids ("bubble pores" or "vugs") is common within individual spray dried feed particles for a variety of reasons (Walker et al., 1999; Bare et al., 2014; Mousa et al., 2023a,b).

* Corresponding author.
E-mail address: sean.rigby@nottingham.ac.uk (S.P. Rigby).

https://doi.org/10.1016/j.ces.2024.120005
Received 20 December 2023; Received in revised form 1 March 2024; Accepted 11 March 2024
Available online 12 March 2024

The aforementioned complexity of pellet fabrication leads to complex final pellet and pore structures. It is generally not initially clear which particular aspects of this process most control the ultimate mass transport properties of the final pellet product, and thus predict key parameters like diffusivities. A so-called "brute force" approach, whereby a complete, direct representation of the whole void space is obtained using an imaging technique, such as CXT or FIB-SEM, followed by simulation of mass transport within that structure using a calculation method, such as the Lattice-Boltzmann approach, that can cope with irregular geometries, can produce accurate predictions of mass transport phenomena and rates for suitable materials (Pavlovskaya et al., 2018). However, the degree of heterogeneity may be such that the correlation length exceeds the size of a pellet, and a single macroscopic (~mm), mesoporous pellet may contain $\sim 10^{15}$ pores, such that all of them cannot be included in a representation of the void space, even with a supercomputer. The degree of spatial heterogeneity introduced during pellet fabrication may be such that there also does not exist a small enough representative volume characteristic of the whole (Nepryahin et al., 2016). Hence, some sort of alternative modelling approach that remains mathematically tractable is often required. Examples of different types of experimental and modelling approaches from previous studies, that illustrate the limitations of accurately representing the void space and attempts to analyse such systems, have been recently reviewed extensively elsewhere (Rigby, 2023). Further, the exact nature and level of simplification of a full image dataset necessary to deliver a tractable model structure is not known in advance (Raeini et al., 2017).

An alternative, classical approach to this problem is to actively select a tractable model type, known as a Galilean idealisation model (Weisberg, 2017; Rigby, 2023), and then add in complexity until the required level is reached. One such model type is a pore bond network (Rieckmann and Keil, 1998; Chen et al., 2008). Unfortunately, there are potential limitations on the accurate representation of pore network features in models, such as the true relative prevalence of macropores amongst mesopores in a bimodal network, as the number of macropores is often sparse compared to the mesoporosity (Hollewand and Gladden, 1992).

However, it is often not necessary to represent a void space exhaustively for the model to be predictive. Kolitcheff et al. (2017) found that literature correlations of tortuosity with porosity gave better agreement with experimental measurements for bimodal pellets, formed from compaction of aggregates of alumina nanocrystals, if only the inter-aggregate porosity was considered, and the porosity within aggregates neglected. This finding was suggestive, but did not actively prove, that mass transport was dominated by the second level of porosity in the hierarchy, since this was not explicitly directly tested. In contrast, the integrated gas sorption and mercury porosimetry method used here allows different sub-sets of the pore network to be physically 'knocked-out', and the impact directly assessed.

Models of the void space network of amorphous catalyst pellets that are just of the degree of complexity required to include the particular causal factors which are responsible for the phenomenon of interest, in this case mass transport, occurring within the porous solid are called minimalist idealisation models (Weisberg, 2017; Rigby, 2023). This type of model only includes those features of the void space structure that 'make a difference to the occurrence or essential character of the phenomenon in question' (Weisberg, 2017), and, therefore, obviates the need for the computationally expensive 'brute force' approach. A way to identify these particular features is a strategy involving actively 'sifting', or 'filtering', out the key aspects of the pellet structure that most determine mass transport rates, to inform the basis of a model (Nepryahin et al., 2016; Rigby, 2020; Hill-Casey et al., 2021). This can be achieved by "knocking-out" only particular features of the void space in a controlled way, and then assessing their impact upon mass transport rates.

In previous work, the sifting strategy, employing entrapment of mercury during porosimetry, or pre-adsorption of water or iodononane, has been used to selectively remove certain pore sizes from the broader pore network, and the impact on the rate of nitrogen or xenon gas uptake measured (Nepryahin et al., 2016; Hill-Casey et al., 2021; Seely et al., 2022; Mousa et al., 2023a,b). If the knock-out agent is of high electron density, like mercury or iodononane, the spatial distribution can be easily imaged using computerised X-ray tomography (CXT) (Nepryahin et al., 2016; Seely et al., 2022; Mousa et al., 2023a,b). If the knock-out agent contains an NMR-active nucleus, then it can be imaged using MRI (Hill-Casey et al., 2021). It is possible to more directly observe the uptake of an electron-rich gas using CXT, as long as sufficient imaging contrast with the solid can be achieved, but this often only arises once the gas condenses out as the stationary denser adsorbed phase and not for the migrating diffuse gas phase itself (Almazán-Almazán et al. (2011); Pini et al., 2021). Even if it were possible to observe the moving gas itself using CXT, it would not also be possible to determine through which particular pores within a voxel the gas is (predominantly) travelling. However, selectively removing certain pores, by filling with an immobile contrast agent, enables their contribution to mass transport to be directly assessed, and their location to be mapped. A fully integrated sequence of gas sorption, mercury porosimetry and multi-modal imaging has been used to study a variety of porous materials, including catalyst supports (Rigby et al., 2004, Mousa et al., 2023a,b), cements (Qian et al., 2018; Zeng et al., 2020; Qi et al., 2021) and rocks (Fusi and Martinez-Martinez, 2013; Seely et al., 2022).

Gas overcondensation is a relatively little-utilised technique in catalysis (Murray et al., 1999; Mousa et al., 2023a,b). However, it means that gas sorption can be used to characterise macroporosity, as well as the usual mesoporosity and microporosity, and thereby provides a unique way to probe all these length-scales with just one technique. This means that the characterisation of a wide range of length-scales is more integrated than attempting to splice together findings from different methods. Overcondensation will be used here to demonstrate the inter-relationship between very large macropores and the smaller pores usually characterised with conventional gas sorption.

In this work, the particular pores critical to mass transport within high temperature shift (HTS) catalyst pellets will be assessed, and their origins in the fabrication process determined, using the sifting strategy. Gas overcondensation will be used to demonstrate the existence of a tri-modal pore network. Mercury porosimetry will be used to selectively entrap mercury within the largest pore sizes, and then progressively smaller ones, in a catalyst pellet. The spatial location of entrapped mercury will be mapped using CXT. The impact on network accessibility and rate of gas uptake will be assessed using serial nitrogen sorption experiments on the same samples before and after mercury entrapment. Differential plots of data from these experiments will provide more statistically-representative findings on pore accessibility than is possible with imaging alone. These data will also be used to develop the minimalist idealised, structural model necessary for representing the macroscopic length-scales of the pellet. In this work, CXT images are not used as the direct 'raw material' for the void space representation, but, rather, for the validation of the model constructed with more indirect characterisation methods. It will be seen that the idiosyncratic model development for a specific material type depends critically on the nature of the particular sifting data. This work will make unconventional use of random cluster (RC) models, with the (normally) 'solid' phase representing the partially blocked (but initially percolating) macroporous network, and the 'void' phase representing the mesoporous matrix through which the former passes. The theoretical prediction from the random cluster model, for the expected change in the mass transport coefficient as a result of the variation in open porosity, will be compared with the experimental findings. Hence, the underlying arrangement of the pore space will be determined, and the critical importance of an incipiently percolating network of macropores to mass transport in the HTS pellets will be demonstrated. The CXT will also make more apparent the origins, in the fabrication procedure, of the key macropore network.

2. Theory

2.1. Mass transport

Mass transport properties can be characterised by kinetic gas uptake experiments. Kinetic mass uptake data, comprising amount adsorbed versus time, typically takes the mathematical form of an exponential growth, and, thus, is often fitted to the so-called Linear Driving Force (LDF) model (Rigby, 2020). The characteristic parameter of this process is the mass transfer coefficient (MTC), denoted k. The LDF k-value is defined by the function (Rigby, 2020):

$$M = M_0\left(1 - e^{-kt}\right) \tag{1}$$

where M is the amount of nitrogen adsorbed at time t, M_0 is the ultimate total adsorbed amount of nitrogen for the adsorption pressure point, and k is the mass transfer coefficient. The apparent mass transfer coefficient, obtained from a fit to raw uptake data, must be corrected for the effect of concurrent adsorption using the slope of the isotherm at the relevant adsorption pressure point. In this way, the actual mass transfer coefficient is obtained.

For a porous sample, the mass transfer coefficient k depends upon the intrinsic effective diffusivity of the porous material, composed of the reference diffusivity D_A, the porosity (voidage fraction), ε, and tortuosity, τ, of the medium, plus the diffusion penetration depth a, and a geometric factor G, which is 15 for a spherical particle and 8 for a cylinder (Rigby, 2020):

$$k = \frac{GD_A\frac{\varepsilon}{\tau}}{a^2} \tag{2}$$

The reference diffusivity will be the bulk molecular diffusivity in the molecular diffusion regime, and the Knudsen diffusivity for the critical pore size in the Knudsen regime. For experiments performed at a constant temperature with the same adsorbate, in the Knudsen regime, the reference diffusivity will be proportional to the critical pore size, r, controlling mass transfer. If the particle overall geometry remains constant, then the ratio of the original mass transfer coefficient k to the subsequent MTC after structural modification will be given by:

$$\frac{k}{k_0} = \frac{\varepsilon}{\varepsilon_0}\frac{\tau_0}{\tau}\frac{r}{r_0}\frac{a_0^2}{a^2} \tag{3}$$

where the subscript 0 denotes the parameter for the original porous network and the lack of subscript represents the general parameter for any modified network.

2.2. Structural model

Prediction of the overall diffusivity for heterogeneous systems is a long-standing problem (Crank, 1975). Prager (1960) developed equations for the overall diffusivity of random systems consisting of two phases with different values of diffusivity. For a system consisting of a volume fraction σ_2 of disconnected, island regions of a phase with a diffusivity of zero randomly distributed amidst a continuous phase of volume fraction σ_1 with diffusivity D_1, Prager (1960) derived the following expression for the overall diffusivity D^e:

$$D^e = D_1\left[\sigma_1\frac{(\sigma_2 + \sigma_1 ln\sigma_1)}{2(\sigma_2 + \sigma_1 ln\sigma_1) - \frac{1}{2}\sigma_1(ln\sigma_1)^2}\right] \tag{4}$$

Given that the isolated phase has zero diffusivity, the patches of it could represent regions of a sample containing disconnected ganglia of entrapped mercury. This model has, thus, been used as a baseline reference to consider the impact of entrapped mercury on mass transport in real samples (Nepryahin et al., 2016; Mousa et al., 2023a,b).

A type of structural model also with a random distribution of impermeable solid phase, but with different topology, is the random cluster (Elias-Kohav et al., 1991). A random cluster is housed on a site lattice, where the sites in the lattice are allocated completely randomly to either solid or void phase, such that the eventual overall fraction of void spaces equals the desired porosity. The complete randomness of allocation means that solid sites may be immediate neighbours, and potentially grow into a percolating network, unlike the Prager (1960) model where the solid remains disconnected. While via different methodologies, Wakao and Smith (1962) and Elias-Kohav et al. (1991) both showed that the tortuosity of a 3D random cluster is related to the porosity by:

$$\tau = \frac{1}{\varepsilon} \tag{5}$$

CXT will be used below to demonstrate that the spatial distribution of pellet constituent feed particles filled with mercury seems random, and, thence, the spatial distribution of the void space regions full of entrapped mercury in them can be modelled as a random cluster structural model, as described above. The mercury saturation, s, is related to the ratio of the porosity following mercury entrapment, ε, to the original pellet porosity, ε_0, by the relation:

$$s = 1 - \frac{\varepsilon}{\varepsilon_0} \tag{6}$$

Hence, if the structure of the pellet containing entrapped mercury can be represented by a random cluster model, such that the tortuosity is related to the porosity via eq. (5), then combining eqs. (5) and (6) gives:

$$\frac{\varepsilon}{\varepsilon_0}\frac{\tau_0}{\tau} = (1 - s)^2 \tag{7}$$

Substituting eq. (7) in eq. (3), and assuming the diffusion penetration depth, a, remains constant, thus gives that the ratio of the MTCs before and after mercury entrapment is given by:

$$\frac{k}{k_0} = \frac{r}{r_0}(1 - s)^2 \tag{8}$$

3. Materials and methods

3.1. Catalyst pellet samples

The catalyst pellet samples used in this work were iron-chromia high-temperature shift (HTS) catalysts supplied by Johnson Matthey, denoted H1-4. The sample characteristics are shown in Table 1. The samples were four development materials, that were all made with slight variations to the manufacturing process, to supply low, medium and high levels of the parameters of porosity, individual pellet (bulk) density, and specific surface area.

3.2. Integrated mercury porosimetry and gas sorption

The integrated mercury porosimetry and gas sorption technique consists of a series of experiments conducted on the same sample. The

Table 1
Characteristic parameters of the HTS catalyst samples studied in this work. The porosity and pellet density were determined from helium-mercury pycnometry.

Sample	Porosity/ %	Pellet density/ (g.cm^{-3})	BET surface area/ (m^{2}g^{-1})	Specific pore volume from bulk/over-condensation /(cm^{3}g^{-1})	Pellet cylindrical dimensions (diameter × length)/mm
H1	52.2	2.44	28.3	0.213	7.0 × 4.0
H2	48.5	2.63	20.3	0.173	7.0 × 4.0
H3	54.9	2.21	27.1	0.203	7.0 × 4.0
H4	44.8	1.92	191.9	0.323	8.0 × 4.0

nitrogen sorption isotherms were measured at liquid nitrogen temperature (77 K) using a Micromeritics 3Flex physisorption analyser. Approximately 0.8 g of the sample (4 cylindrical pellets) was weighed and placed into a pre-weighed standard physisorption sample tube with a sealing frit placed at the top to prevent the sample from being evacuated into the 3Flex manifold. The tube (with sample) was then loaded into the degassing station and initially degassed at room temperature until a vacuum of 0.02 mmHg was reached. The sample temperature was then raised to 140 °C by using a heating mantle, and the sample was left under vacuum for 24 h. The thermal pre-treatment drives off any physisorbed water on the sample but does not change the sample morphology. After the 24 h had passed, the heating mantle was removed, and the sample was allowed to cool down to room temperature. The sample tube and its contents were then re-weighed to obtain the dry weight of the sample. Isothermal jackets were then placed around the sample tubes before reattaching them to the analysis port to begin the automated gas sorption analysis. The isothermal jacket ensures a constant thermal profile of 77 K along the length of the sample tube during the analysis stage. Nitrogen purity was 99.995 %. The isotherms consisted of approximately 60 adsorption and 50 desorption points. Gas sorption was measured over the relative pressure (P/P_0) range of 0.01 to 0.995 for the adsorption isotherm and 0.995 to 0.10 for the desorption isotherm. The saturation pressure (P_0) was measured for each data point on the isotherm.

Once the first nitrogen gas sorption experiment was finished, the samples were allowed to reach room temperature (~295.15 K) and then quickly transferred to a mercury intrusion porosimetry (MIP) machine to entrap mercury into the pores. Mercury intrusion and retraction curves were measured using a Micromeritics Autopore IV 9500, which can generate a maximum pressure of 414 MPa (60,000 psia). Mercury intrusion data was generated for the range specified in the scanning curve pressure points followed by retraction back down to atmospheric pressure. The sample was transferred into a penetrometer, and the weight of the penetrometer and sample was recorded. The penetrometer (with sample) is then placed in the low-pressure port of the instrument. During the low-pressure analysis, the sample is evacuated down to 50 μmHg to drive off any water vapour or atmospheric gases in the pore network. The sample bulb is then filled with mercury while the entire system is still under low pressure. Data collection begins at a pressure of 0.5 psia, which is enough to cause mercury to penetrate sample pores larger than 360 μm in diameter. After the low-pressure analysis was completed, the assembly weight (penetrometer + sample + mercury) was recorded, and the penetrometer was transferred to the high-pressure port, and the chamber was closed tightly. The penetrometer is placed vertically in the high-pressure port, and it is surrounded by oil, which is the hydraulic fluid the instrument uses to generate high pressures. As the hydraulic fluid pressure rises, it is transmitted to the mercury in the penetrometer via its open capillary stem. An equilibration time of 15 s was used for each data point.

Once the mercury intrusion experiment was finished, the sample was immediately discharged from the penetrometer, recovered, and returned to the 3Flex sample tube, where the rate of adsorption and the conventional adsorption experiments were repeated. The sample was first cooled to 77 K by manually raising the Dewar flask, allowing the sample to freeze for approximately 30 min. This part was crucial in the post mercury entrapment steps since it freezes the mercury in-place to ensure that it all remains immobilised within the pellets. The integrated rate of adsorption-mercury porosimetry aims to selectively block specific pore sizes and then study how important those pores were to the rate of mass transport before and after their removal. Previous experiments where the mercury was thawed and re-frozen after a week prior to subsequent gas sorption have shown that the mercury ganglia did not move around over this timescale or due to the freezing since the shapes of the gas sorption isotherms remained the same (Nepryahin et al., 2016).

Potential damage to the sample, due to the high pressures involved in the mercury porosimetry experiment, can manifest in a number of ways that can be tested for. For example, sample damage can look like apparent mercury entrapment if the sample is simply crushed. However, true mercury entrapment can be detected by a commensurate weight gain for the sample after mercury porosimetry, and this was observed by weighing the sample post porosimetry.

3.3. Overcondensation gas sorption procedure

The nitrogen overcondensation (OC) experiment was carried out on a Micromeritics ASAP 2020 physisorption analyser. The OC experiment is explained in more detail in previous work (Mousa et al., 2023a,b) and uses a method similar to that described by Murray et al. (1999). The OC experiment involves "flooding" the sample chamber with condensed liquid nitrogen to submerge the sample in liquid nitrogen to investigate any porosity beyond the instrument upper limit for the conventional isotherm ($P/P_0 > 0.995$). The conventional isotherms for these materials clearly show that porosity exists beyond the conventional instrument's upper limit. Once the sample is fully submerged in liquid nitrogen and total pore filling is achieved, the pressure in the tube is lowered to just below the saturated vapour pressure of nitrogen such that the bulk condensate vapourised completely while all the sample internal porosity is liquid-filled. Once this step has been achieved, the first data point on the overcondensation desorption isotherm can be measured. This point corresponds to the total pore volume of the sample. The pressure is then progressively lowered in small steps, and the rest of the desorption isotherm was obtained in the usual way. The reported raw data (relative pressure and volume adsorbed (cc/g STP)) is greatly offset to what would be expected due to the very large amount of gas (from the bulk liquid nitrogen) that must be removed before the onset of desorption from the sample porosity. The data were normalised to a quantity of gas on the adsorption isotherm below a relative pressure of 0.42 where, for the conventional isotherm, the desorption data coincides with the adsorption data. The OC data was collected for the samples both before and after mercury intrusion.

3.4. Rate of adsorption (ROA) procedure

The rate of adsorption technique works by dosing a known quantity of nitrogen gas onto the sample and then recording the amount of gas adsorbed, and the corresponding pressures, over time. The dosing quantity was taken from the BET monolayer capacity (V_m). An additional 5 cc of gas was added to this amount to compensate for the initial expansion of the gas into the free space of the sample tube. This is because the gas first fills the sample tube before adsorbing onto the sample surface. The number of readings of pressure was set at 1000 readings per dose. The ROA data was collected at the lowest pressure point in the isotherm. In this region of the isotherm, there is negligible obstruction from adsorbed phase, and the diffusion is in the Knudsen regime and corresponds to the process conditions in the reactors in which many types of pellets are used. The rate of uptake data was collected both before and after mercury entrapment.

3.5. Computerised X-ray tomography (CXT)

For the CXT scans, the pellets were imaged before and after mercury entrapment using a Zeiss Xradia Versa XRM-500 to acquire 3D image stacks. The X-ray source for the Xradia 500 Versa instrument was set to 140 kV and power of 10 W. The apparatus's macro lens (0.4X) was used to image the whole pellets with 360 degrees rotations. The average pixel size for empty pellets was 4.5 μm, and the average pixel size for samples with mercury was 8.5 μm. The scan times were roughly 2 h for the empty samples and 2.5 h for mercury-filled pellets. Both types of samples were scanned with 1600 projections per 360 degrees scan. Each 3D image stack contained 1016 slices with dimensions of 1024 × 1024 pixels and 24-bit depth.

3.6. Image analysis

The aim of the CXT analysis post-mercury injection was not to delineate the precise pore sizes infiltrated by mercury, given that these sizes often fall below the resolution limit of the CXT used, but, rather, to map the spatial distribution of regions within the catalyst pellet that exhibit significant mercury intrusion versus those with minimal or no intrusion. To achieve this, we utilized a convolutional neural network (CNN) model, specifically tailored to recognize and segment based on the changes in brightness and texture that mercury intrusion induces in the CXT images. This approach leverages the subtle yet discernible alterations in image characteristics caused by the presence of mercury, rather than attempting to quantify the exact sizes of the mercury-filled pores. The segmentation process, therefore, focuses on differentiating between high-density (mercury-intruded) and low-density (unintruded or minimally intruded) regions within the pellet, effectively mapping the spatial variation in mercury distribution.

A flowchart detailing the image analysis and segmentation steps utilized in this study is given in the Supplementary Material as Figure S1 (a). The image analysis and segmentation for high-temperature shift (HTS) catalyst samples, following mercury injection, utilized Dragonfly ORS software, employing a deep learning neural network (Makovetsky

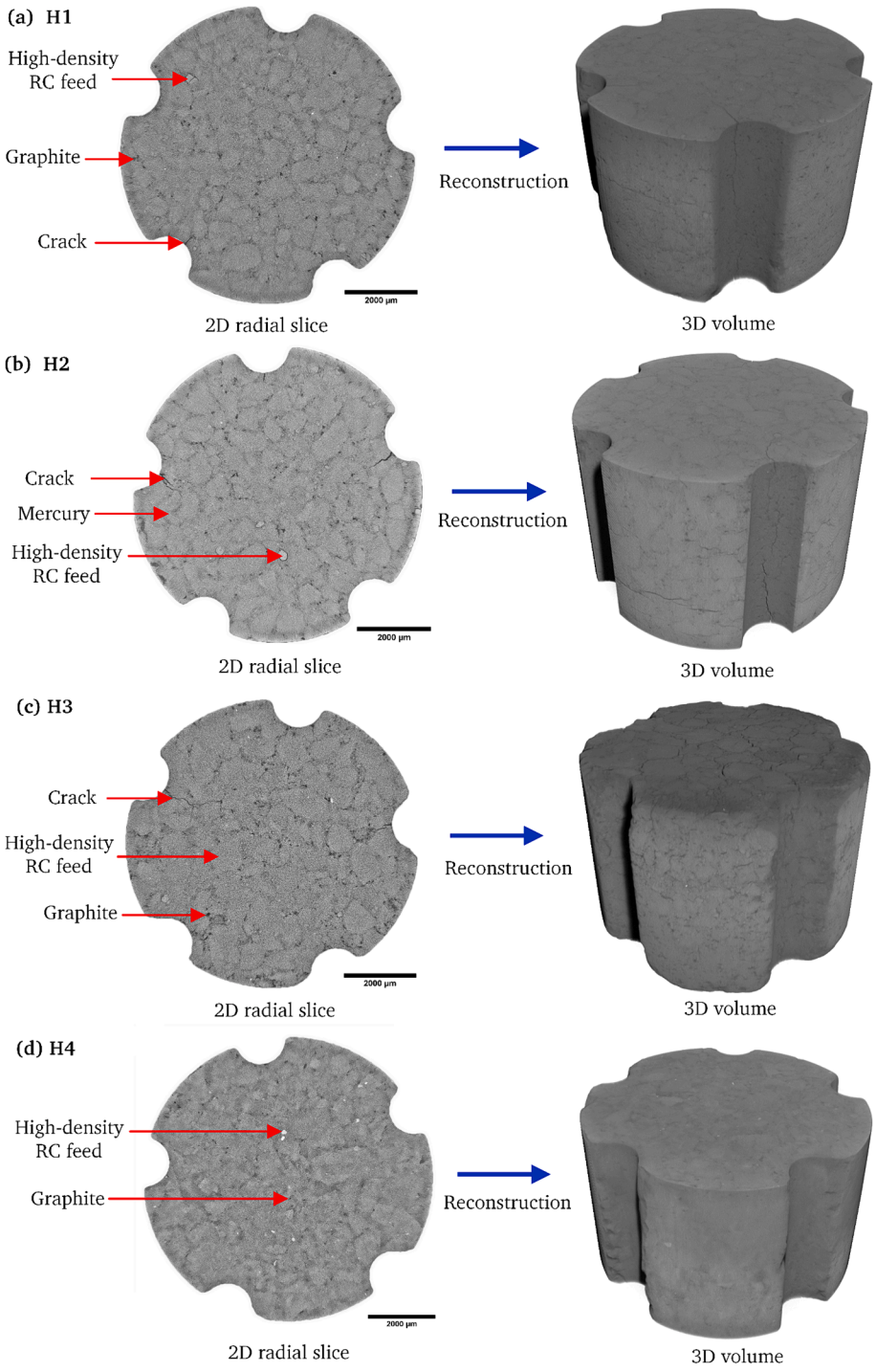

Fig. 1. Typical CXT 2D slice images of the middle region of a pellet, together with full 3D reconstructions of the pellets, for each of sample H1(a), H2(b), H3(c) and H4(d). (here RC = roll-compacted).

et al., 2018). A U-Net convolutional neural network (Ronneberger et al., 2015) was specifically configured for segmenting mercury-filled images, with a 32 × 32 pixel patch size, a stride-to-input ratio of 0.5, a batch size of 32, using 'OrsDiceLoss' as the loss function, and optimized with Adadelta (Zeiler, 2012). The pre-processing phase was critical, involving extensive noise reduction and contrast adjustments through Fiji software, applying filters such as CLAHE and a non-local means filter for edge preservation, essential for highlighting subtle brightness changes due to mercury infiltration.

Figure S1(b), in the Supplementary Material, shows an example raw CXT image and a chart showing the histogram of pixel grey levels. It can be seen that the distribution of pixel intensities is bimodal, with two clear peaks corresponding to the mercury-containing and empty image pixels, which made the segmentation procedure unambiguous. For the U-Net model training, 20 out of 1016 pre-processed 2D image slices were carefully delineated to classify each pixel, effectively distinguishing between empty and mercury-filled regions. This detailed manual segmentation, supported by Dragonfly's comprehensive toolkit including brushes and erasers, formed a solid training dataset. The model reached an accuracy of 85 % after 35 epochs, improving to 97 % after 100 epochs. However, this high accuracy did not entirely preclude errors in automated segmentation on previously unseen images, where isolated clusters of inaccurately labelled pixels were noted, such as low-density regions mistakenly identified as high-density. These inaccuracies were rectified in post-segmentation processing, ensuring the fidelity of the final segmented stacks. The segmentation's accuracy was visually validated by comparing selected segmented slices against their original counterparts, affirming the model's precision in identifying different phases within the HTS catalyst pellets.

4. Results and discussion

4.1. CXT of fresh empty samples

CXT of the fresh samples was used to study the internal structure of the pellets resulting from their fabrication method. Fig. 1 shows typical 2D slice images of the middle region of pellets from each batch, together with full 3D reconstructions of the pellets. From the images given in Fig. 1, it can be seen that the pellets of all four different samples are all made up of irregular polygonal, roll-compacted feed particles of typical sizes of the order ~ 100–1000 μm. The feed particles are of variable density, as shown by the variation in pixel intensity between feed particles, which indicates that the X-ray absorbance differed between feed particles. The pellets thus contain high-density and low-density feed particles, and, also, smaller, dark black spots that correspond to graphite lubricant particles. The CXT images also show that the pellets possess some large macropores, as indicated by the low X-ray absorbance irregular lines crossing the pellets. The low-density sample H3 seems to have more of these macropores than the other samples, while H4 has much less macropores visible in the CXT images compared with the other samples. The CXT data suggest that the individual feed particles still remain individually identifiable in the composite body, and the pelleting process has led to some induced macroporosity.

4.2. Mercury porosimetry

Raw mercury porosimetry curves were obtained for intrusion up to 60,000 psia (414 MPa), and then retraction back down to ambient. These raw data were analysed using the Kloubek (1981) correlations, which are a version of the Washburn equation where the surface tension and contact angle terms have been calibrated for pore size. The analysed data are shown in Figure S2 in the Supplementary Material. From these data, it was seen that there is an initial small step for sizes > 10,000 nm corresponding to intrusion into gaps between the pellets. Thereafter there is a long flat plateau before substantial mercury intrudes the sample at neck sizes ~ 10–200 nm. The intrusion is bimodal in all cases, with a second intrusion mode in the range ~ 3–20 nm, depending upon sample. For the retraction, there is almost 100 % entrapment for all samples. This 100 % entrapment for HTS samples means that mercury behaves just like the low melting point alloys used in previous work (Cody and Davis, 1991; Ruffino et al., 2005), but without the need for both heating and cooling the alloy.

Mercury porosimetry scanning curves were also performed with various ultimate intrusion pressures from 7000 psia to 1200 psia for samples H1-3, and 5336 psia and 3800 psia for sample H4, as shown in Table 2. In particular, the pressure of 5336 psia was chosen as this corresponds to the region of break-of-slope between the two intrusion modes for samples H1-3. It also corresponds roughly to the point of inflexion in the large pore size modal step for sample H4. Further, the lower ultimate intrusion pressure of 1200 psia was chosen for the second scanning curve to correspond to roughly the point of inflexion of the large pore size intrusion step for samples H1-3. The mercury porosimetry data for selected scanning curve experiments, analysed using the Kloubek correlations, are shown in Figure S2 in the Supplementary Material. It can be seen that, within some minor intra-batch variability, the mercury intrusion curves are repeatable between runs. It can also be seen from Figure S2, that the scanning curves also result in very close to ~ 100 % mercury entrapment. Hence, the pores intruded (as given in Table 2) are also the ones blocked by entrapped mercury as there is no mercury withdrawal. The mercury saturation levels (based upon the mercury porosimetry pore volume) thereby achieved are shown in Table 2.

Mercury porosimetry experiments, with intrusion up to 60,000 psia, were also performed on samples H1-4 after the pellets had been fragmented to powder of particle sizes 50–75 μm. This particular particle size was chosen such that it was smaller than that of the roll-compacted feed particles seen in Fig. 1. Due to the increased mercury intrusion in the gaps between powder particles for fragmented samples, in order to facilitate better comparison between the whole and powder samples, the ultimate intrusion volume for the powder data was renormalized to that of the corresponding whole pellet sample. The two data-sets for each sample are compared in Figure S3 in the Supplementary Material. From these data it was seen that the shapes of the intrusion curves for the whole pellet and corresponding powder samples are generally very similar. This suggests that fragmentation of the pellet to this particle size does not produce any large shift in the intrusion curve towards lower pressure (larger pore size), and, thence, there is little, or no, deshielding due to fragmentation. However, there is a slight shift at the very bottom of the intrusion curves for samples H1 and H3, corresponding to a slight deshielding of the very largest pore sizes. There is also a slight shift for the small pore size mode in the intrusion curve for sample H2, but not the larger pore sizes.

4.3. CXT of pellets following mercury porosimetry

CXT of pellets following mercury entrapment, resulting from porosimetry scanning curves, was used to probe macroscopic heterogeneities in the spatial distribution of mercury intrusion, and assess their spatial pattern. Pellets from samples H1-4 were imaged with CXT following mercury intrusion to the particular ultimate pressures shown in Figure S2. Since mercury entrapment approached 100 % in all cases, it can be expected that entrapped mercury visible in CXT images is located only in intruded pores. The images shown in this section were obtained as immediately after discharge from the porosimeter as possible (within hours), but images were repeated a week later, and no obvious migration in entrapped mercury was observed. Examples of image data for single pellets following intrusion to 1200 psia for samples H1-3, and to 3800 psia for sample H4, are shown in Figs. 2-5. From the 2D slice and reconstructed 3D volume images, it can be seen that, at these intrusion pressures, the entrapped mercury has filled the sample-spanning macroporosity, as indicated by the bright white irregular lines seen in the images. However, it can also be seen that the level of mercury intrusion

Table 2
Fractional mercury entrapment, and overall mercury saturation, calculated from mercury porosimetry data (based upon maximum mercury intrusion volume), and from conventional nitrogen adsorption isotherm data, respectively, following partial intrusion to listed pressures. Also shown is the ratio of the volume-weighted average pore diameter after mercury entrapment to that before, obtained from the Barrett-Joyner-Halenda (BJH) (Barrett et al., 1951) adsorption isotherm pore size distribution.

Mercury intrusion pressure /psia	Corresponding pore radius from Kloubek (1981) correlations /nm	Sample	Fractional mercury entrapment /%	Fractional mercury saturation from Gurvitch volumes/%	Ratio of volume weighted average BJH adsorption pore diameter after Hg to before
1200	73.1	H1	20.1	10.0	1.0
		H2	21.2	7.96	0.993
		H3	18.2	11.8	0.977
3800	23.1	H4	9.6	13.9	1.0
5336	16.4	H1	44.3	20.3	0.721
		H2	46.3	28.3	0.719
		H3	56.1	34.7	0.543
		H4	39.8	28.7	1.0
5750	15.3	H2	54.1	37.6	0.68
5900	14.9	H2	58.2	52.0	0.643
6500	13.5	H3	65.1	56.3	0.600
7000	12.5	H1	78.7	74.0	0.727

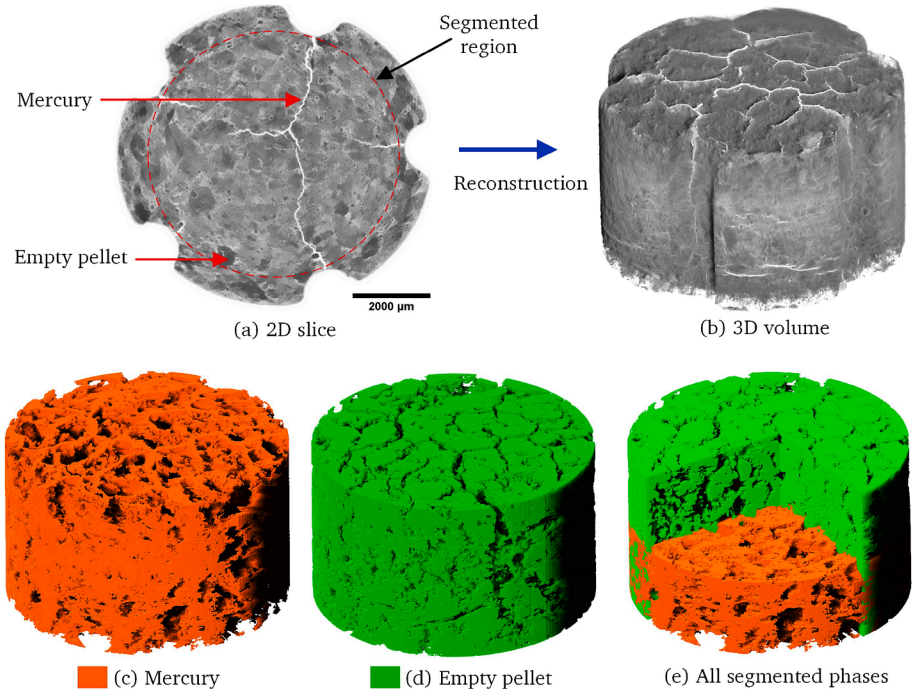

Fig. 2. Example of 2D slice CXT image (a), 3D volume reconstruction (b), and segmented image showing mercury-containing regions (c), regions of pellet empty of mercury (d), and combined phases (e) for sample H1 following mercury intrusion to 1200 psia.

of individual roll-compacted feed particles, as indicated by grey-level, tends to be either very high, creating brighter, whiter voxels, or very low, leaving very dark voxels (see also Supplementary Material Figure S1(b)). This contrast in mercury entrapment between feed particles facilitated further image analysis. Figs. 2-5 also show the results of image processing involving segmentation. The images were segmented into two bins of voxel intensity corresponding to mercury containing and the empty regions of the pellets using deep learning imaging segmentation. The deep learning method utilised here is based on the software Dragonfly from ORS, which uses the popular TensorFlow deep learning engine in a user-friendly image processing environment. Due to the complex overall shape of the HTS pellets, it was not possible to carry out segmentation on the entire pellet image, and so, therefore, the CXT images of the HTS pellets were cropped to extract a central cylindrical volume. The middle regions of the pellets chosen for the segmentation processing are highlighted with a circle (red dashed line) in Figs. 2-5. The volume fractions of this cylindrical volume identified as containing entrapped mercury, and unfilled are given in Table 3.

From Figs. 2-5, it can be seen that the regions of the pellet identified as mercury-containing or empty tend to have the same irregular, polygonal shapes as the roll-compacted feed particles observed within fresh, empty pellets in the images in Fig. 1. The spatial distribution of largely empty and largely filled feed particles seems random.

5. Gas sorption

Conventional gas sorption isotherms, for the HTS pellets before and after mercury entrapment following intrusion up to different pressures, were obtained and are given in the Supplementary Material (Figure S4). The isotherms for the H1 to H3 samples before mercury porosimetry were found to have similar shapes but different ultimate amounts of gas adsorbed. The quantity of gas adsorbed is relatively small until a relative

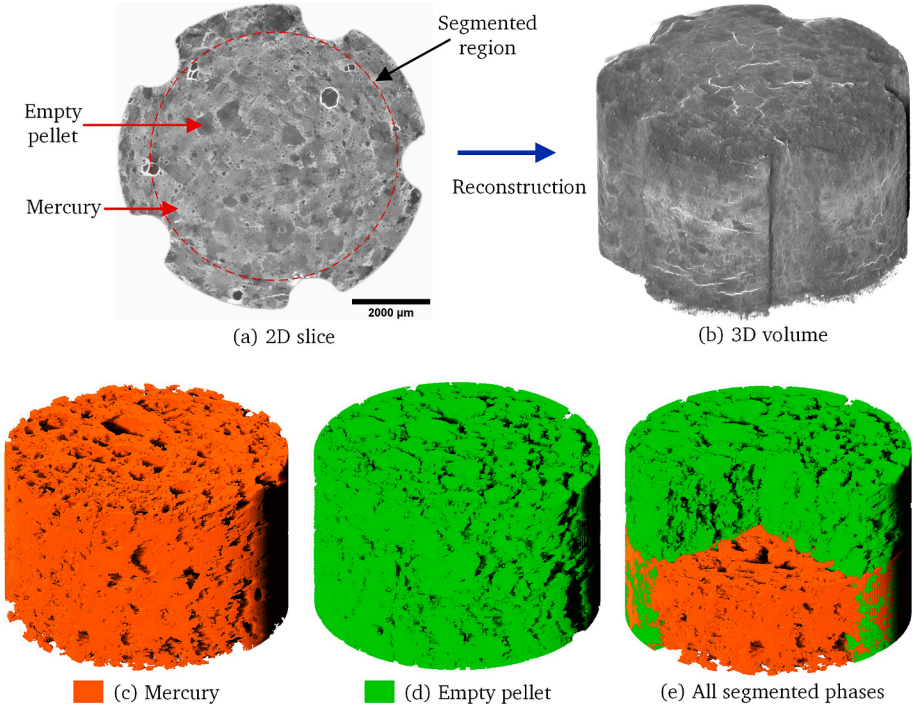

Fig. 3. Example of 2D slice CXT image (a), 3D volume reconstruction (b), and segmented image showing mercury-containing regions (c), regions of pellet empty of mercury (d), and combined phases (e) for sample H2 following mercury intrusion to 1200 psia.

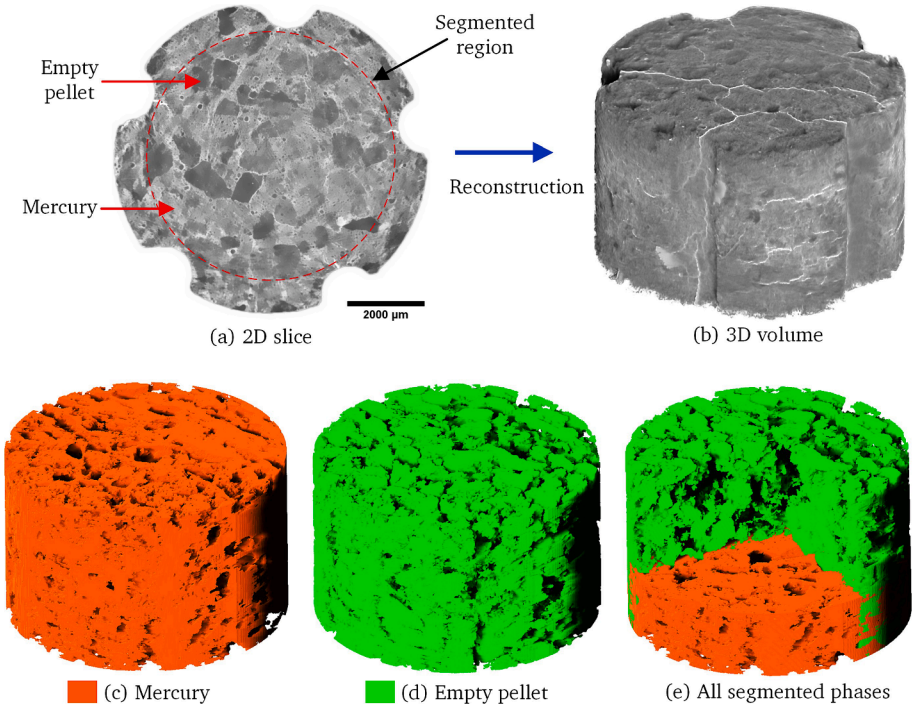

Fig. 4. Example of 2D slice CXT image (a), 3D volume reconstruction (b), and segmented image showing mercury-containing regions (c), regions of pellet empty of mercury (d), and combined phases (e) for sample H3 following mercury intrusion to 1200 psia.

pressure of ~0.8, and is due to multi-layer build-up. However, at a relative pressure ~0.8–0.82, capillary condensation in the pores starts and continues up to a relative pressure of ~0.995. The boundary adsorption isotherms for the H1 to H4 samples have plateaued at a relative pressure ~0.995, suggesting that all the pores have been filled with condensate at the highest relative pressure possible in a conventional gas adsorption experiment. Hence, the apparent mercury saturation was calculated from the fractional change in total (Gurvitch) pore volume accessible to adsorbing nitrogen, and the results are shown in Table 2. From Table 2, it can be seen that the fractional accessible pore volume, as measured from conventional nitrogen adsorption, is typically less than the mercury saturation calculated from the porosimetry data itself. The reason for this discrepancy will be discussed below.

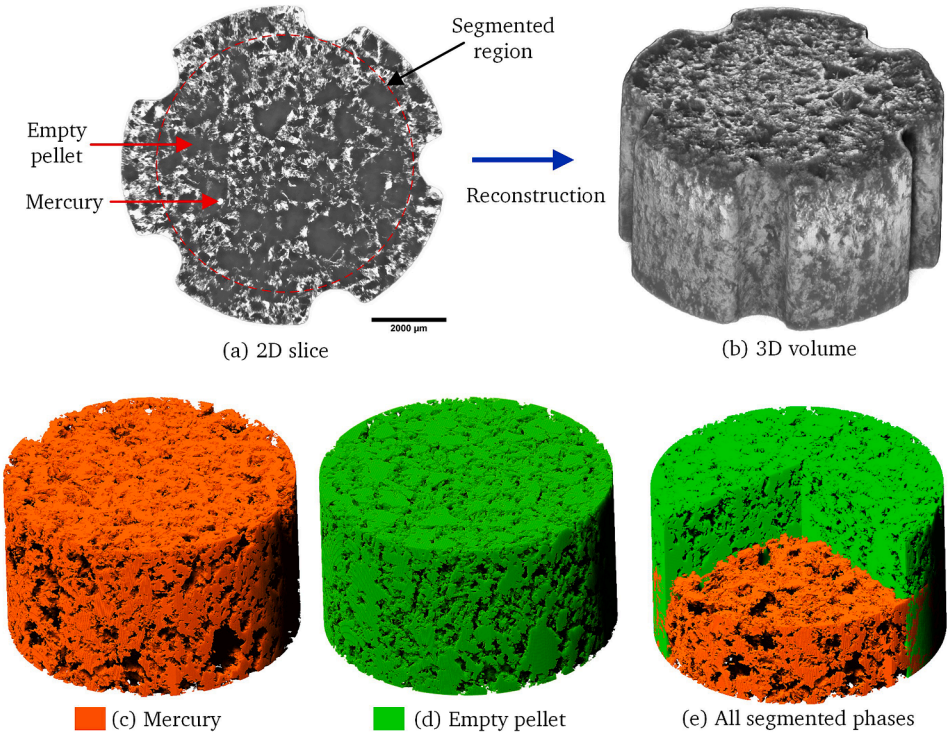

Fig. 5. Example of 2D slice CXT image (a), 3D volume reconstruction (b), and segmented image showing mercury-containing regions (c), regions of pellet empty of mercury (d), and combined phases (e) for sample H4 following mercury intrusion to 3800 psia.

Table 3
Volume fractions of two phases (mercury-containing and empty) identified using the image segmentation algorithm for images in Figs. 4-7.

Sample	Volume fraction of mercury-containing phase/%	Volume fraction of empty phase/%
H1	42.8	57.2
H2	51.7	48.3
H3	60.3	39.7
H4	37.5	62.5

The desorption isotherms for samples H1-3 exhibit two knees, one at a relative pressure ~0.98, and a second percolation knee at relative pressure ~0.9–0.92. After this second knee, the capillary evaporation continues to the hysteresis closure point at a relative pressure of ~0.85. The overall form of the hysteresis loops for samples H1-3 is suggestive of two zones, above and below the kink in the mid-section of the hysteresis loop. In the lower pressure zone, the hysteresis loop is more rectangular in form with parallel, nearer vertical adsorption and desorption boundary curves, while the boundary curves of the upper zone appear to converge more and are at a more pronounced angle to the vertical. The hysteresis loop for Sample H4 does not possess this same form.

Gas overcondensation experiments were used to study the larger macropores in the pellets. Nitrogen overcondensation (OC) experiments were also performed on empty pellets of samples H1-H4 and the OC boundary desorption isotherms thereby obtained were compared with the corresponding conventional sorption isotherms for the same sample. Examples of these data for samples H1 and H4 are shown in Fig. 6. The corresponding data for samples H2 and H3 were of similar overall form to that for H1, and are, thus, given in the Supplementary Material (Figure S5). The sharp vertical drop in the OC isotherm at the highest relative pressure represents evaporation of bulk condensate from the sample chamber outside the pellets, and the end of this drop corresponds to the point of complete pore filling of the pellets with liquid condensate. The specific pore volumes for the samples H1-4 calculated from this point are given in Table 1. It is noted that the sample pore volumes obtained from overcondensation are very similar to the corresponding values obtained from mercury intrusion porosimetry, as shown in Figure S2. This suggests that the nitrogen overcondensation and mercury intrusion probe the same void spaces. From Fig. 6, it can be seen that the top of the OC desorption isotherm has a larger amount adsorbed than that for the clear horizontal plateaus at the top of the conventional adsorption isotherms (CAIs). This suggests that some pores in the pellet must only fill with condensed nitrogen in the range of relative pressures above the last point of the CAIs, namely ~ 0.995–1. It is noted that relative pressures of >~0.998 correspond roughly to >~1 µm from the Kelvin equation. Hence, it seems likely that the pores that are filled at the top of the OC desorption isotherm but not at the top of the CAI are the very large macropores of diameters of the order of a few microns visible in the CXT images of the pellets in Figs. 1 and 2-5. However, given the deviation of the OC boundary desorption isotherm from the conventional desorption isotherm (seen in Fig. 6) extends even down to relative pressures of ~ 0.97 for some samples, this suggests that some of these very large macropores are still shielded by much smaller necks of sizes ~ 10s-100s nm. This is now also made evident from the mercury intrusion curves in Figure S2. However, the tri-modal nature of the pore size distribution (PSD) in the pellets would not have been made evident without the comparison of the OC isotherms and CAIs, as described above, due to the pore shielding effect. Therefore, in summary, there are three main modes in the PSD, first the very large macropores seen in the CXT images, second the intermediate-sized macropores responsible for the upper zone of the conventional gas sorption data, and, third, the mespores responsible for the wide, lower pressure hysteresis loop in the nitrogen sorption data.

In the nitrogen sorption isotherm data in Figure S4 for samples H1-3 following mercury intrusion to a low pressure of 1200 psia, generally, the overall form of, and the amount adsorbed in, the lower zone of the hysteresis loop is retained, but the angle of tilt from the vertical of the upper zone increases as less is adsorbed overall. Following mercury intrusion to 5336 psia, for samples H1 and H2, the whole of the upper zone of the hysteresis loop is lost, but the form and size of the lower zone is retained. For sample H3, the whole of the upper zone has also been

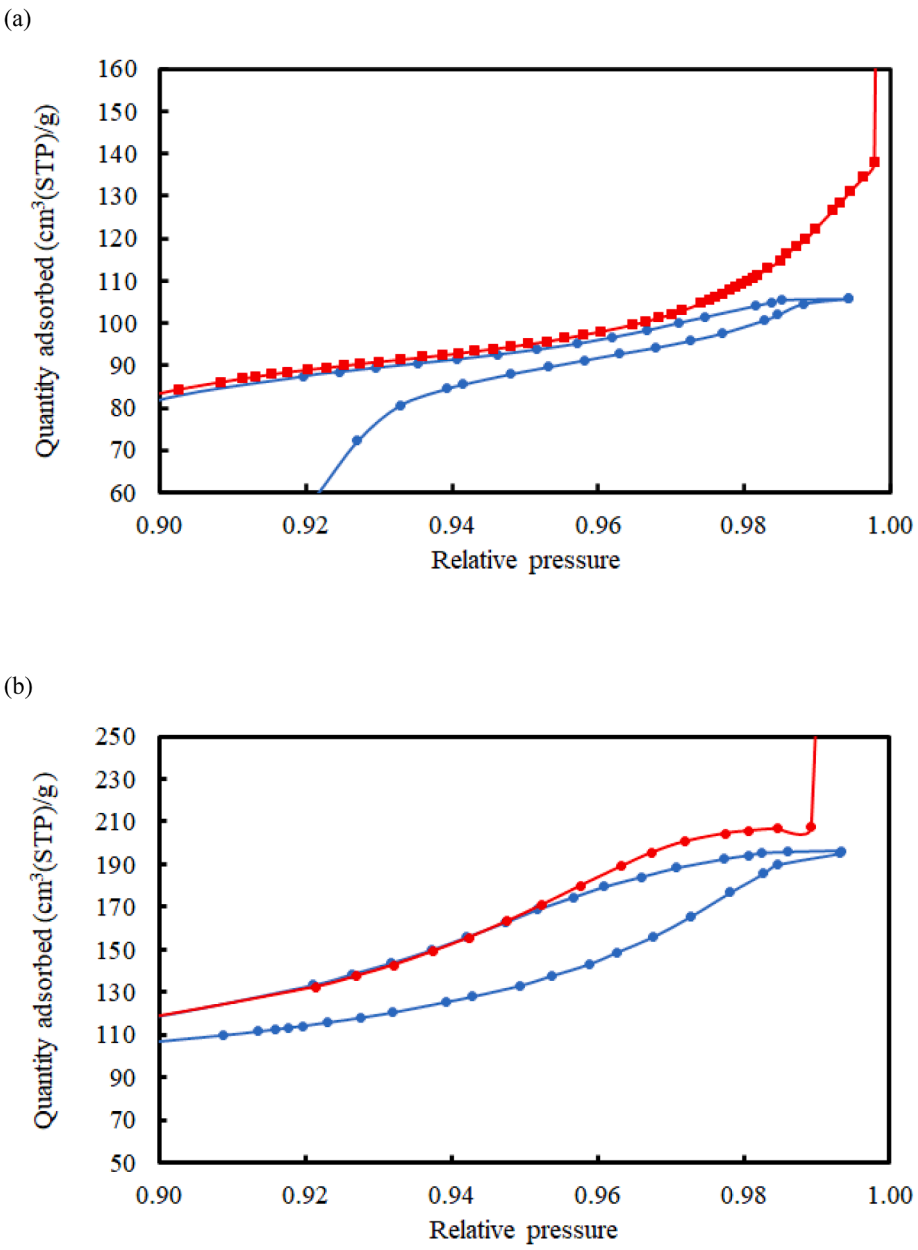

Fig. 6. Examples of comparisons of the upper region of the overcondensation boundary desorption (■) with the conventional sorption isotherms (●) for empty samples of (a) H1 and (b) H4.

lost, but, in addition, the top of the lower zone has been truncated, although the hysteresis width of the remainder is retained. For sample H4 the overall form and width of the hysteresis loop is retained, as progressively more mercury is entrapped, but overall amount adsorbed declines.

The form of the hysteresis loops was investigated further to infer information on the nature of the intermediate macropore network. The isotherm data after mercury intrusion to 5336 psia, in Figure S4, was subtracted from that for the empty sample. An example of such a difference plot is shown in Fig. 7(a) for sample H3. It can be seen that the subtraction process effectively abstracts the top zone of the hysteresis loop from the remainder. The individual relative pressures for each of the adsorption data-points were all squared, and the resultant new adsorption isotherm is also shown in Fig. 7(a). It can be seen that the new adsorption isotherm then becomes superposed upon the desorption data, and the hysteresis loop is closed. This suggests that the hysteresis is of solely single pore origin, as in the Cohan (1938) equations and density functional theory (Neimark and Ravikovitch, 2001), and had no apparent pore-shielding contribution. This means that the intermediate-sized macropores in the percolating network are located more towards the exterior of the sample or near the very largest macropores of the first size mode, and/or that any corrugations along the length of the macropore network do not exceed the critical size ratio for advanced condensation to occur in shielded larger pore sizes. As shown in previous work (Hitchcock et al., 2014), through ink-bottle type pores (or corrugations in a longer pore chain) can behave like straight cylindrical pores if the pore body to neck size ratio does not exceed the critical value for advanced condensation in the pore body. This is because then the pore neck size controls both adsorption and desorption pressures, and the hysteresis width is that expected for a cylindrical pore open at both ends, as given by the Cohan (1938) equations (or similar).

Fig. 7(b) shows the raw sorption data for sample H3 following mercury intrusion to 5336 psia, and also adsorption data where the individual relative pressures have been adjusted by raising to the powers

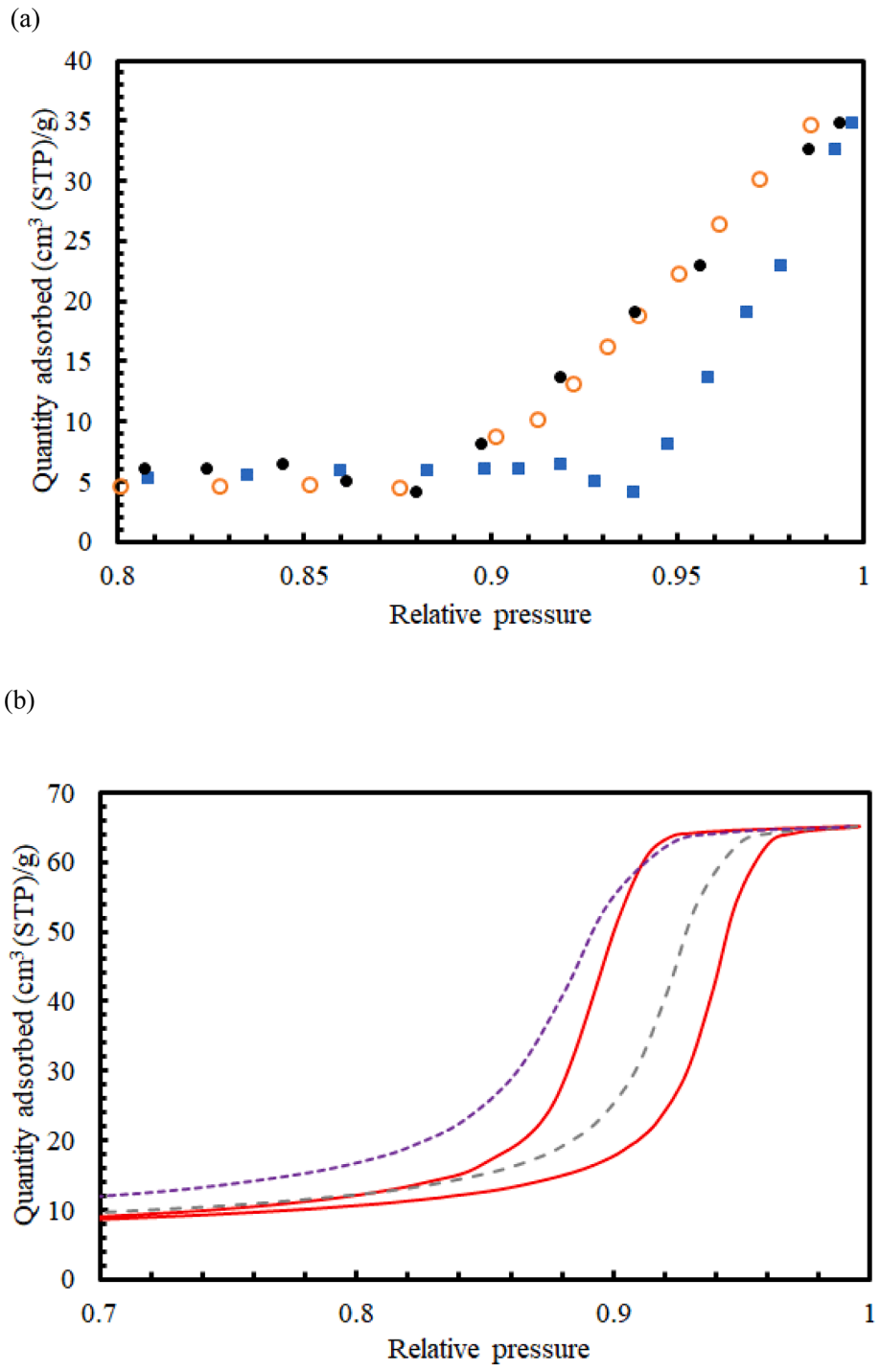

Fig. 7. (a) Plot of resultant adsorption (■) and desorption (○) data following subtraction of isotherm after mercury intrusion to 5335 psia from isotherm for empty sample of H3, together with the adsorption data where the relative pressures have been raised to a power of 2 (●). (b) Comparison of original sorption data (red solid line), for sample H3 following mercury intrusion to 5336 psia, with modified adsorption curves constructed by raising relative pressure to power of 1.3 (grey dashed line) or 2.0 (purple dotted line).

of 1.3 or 2.0. It can be seen that, in contrast, to the upper zone of the hysteresis loop, neither of these powers leads to a complete superposition of the adsorption upon the desorption data. However, it is noted that the adsorption isotherm raised to the power of 1.3 smoothly re-joins the desorption isotherm at relative pressures around ~ 0.8. A comparison of the findings in Fig. 7(a) and (b) suggests that the hysteresis width is different, and has varying causes in the lower and upper zones of the loop, since the powers to achieve superposition of adsorption on desorption are different. The hysteresis in the lower part of the isotherms has a different origin to that of the upper part discussed above. It is likely that the lower part includes some structural hysteresis due to pore network effects, indicating a more complex void space.

A detailed study of the changes in the nitrogen sorption hysteresis following mercury porosimetry was used to provide pore-scale information on where mercury was becoming entrapped and the relative juxtaposition of pores of different sizes. Fig. 8(a) shows the conventional and overcondensation nitrogen sorption isotherms for an empty sample of H1, and the conventional sorption isotherms obtained after mercury

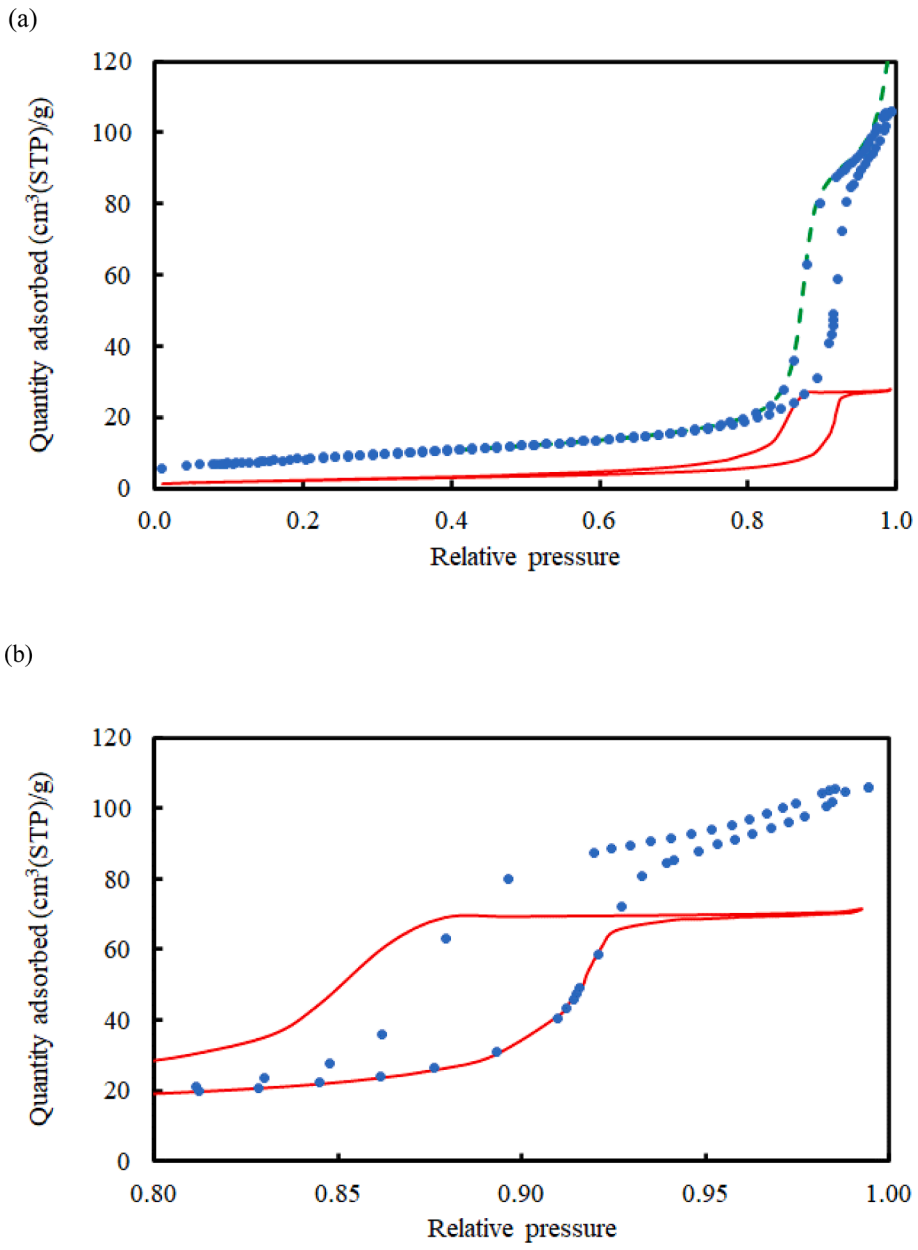

Fig. 8. (a) Comparison of the conventional (blue ●) and overcondensation (green dashed line) nitrogen sorption isotherms for an empty sample of H1, and the conventional sorption isotherms (red solid line) obtained after mercury intrusion, of the same sample, to 7000 psia. (b) Comparison of the conventional nitrogen sorption isotherms for an empty sample of H1 (blue ●), and for the same sample after mercury intrusion to 7000 psia (red solid line) but where the amount adsorbed data shown in (a) have each been multiplied by a factor of 2.35 and a constant volume of 6 cm^3g^{-1} added.

intrusion to 7000 psia. It can be seen that the entrapped mercury leads to a substantial drop in the amount adsorbed. However, Fig. 8(b) shows a comparison of the same conventional nitrogen sorption isotherms for the empty sample of H1, but where the data for the same sample after mercury intrusion to 7000 psia has now had the amount adsorbed multiplied by a factor of 2.35 and a constant volume of 6 cm^3g^{-1} added. From Fig. 8(b), it can be seen that this transformation of the latter data leads to a good superposition of the adsorption isotherm obtained after mercury entrapment onto that obtained beforehand. The constant volume of 6 cm^3g^{-1} added represents the loss of multilayer adsorption from the macropore mode filled with entrapped mercury. The fact that the good superposition of the capillary condensation region can be achieved with a single factor suggests that the entrapment of mercury leads to a loss of pore sizes across the range of the mesopore mode, generally in the proportions originally present in the empty sample, except for the largest mesopore sizes since the top of the hysteresis loop after entrapment is truncated. The mercury intrusion pressure of 7000 psia corresponds to a pore diameter of 26 nm from the Kloubek (1981) correlation, which, in turn, corresponds to a condensation relative pressure of ~ 0.92 for a hemispherical meniscus from the Cohan (1938) equation, which is similar to where the scaled post mercury adsorption isotherm diverges from the before mercury isotherm. This suggests that all of the pores larger than the size corresponding to the ultimate mercury intrusion pressure in the scanning curve have been lost.

However, the loss of a fraction (~4/7) of the rest of the pore sizes too also suggests that the different neck sizes progressively penetrated by mercury generally guard access to the near full range of pore sizes. Seaton (1991) proposed that, in random networks, pores that belong to the (invasion) percolating cluster (in this case corresponding to mercury intruded pores) are only distinguished from other pores above the critical pore size (for intrusion) by their location alone, and so their pore size distribution will be the same for both. The large range of

superposition of the adsorption isotherms (and thus similarity in accessible pore size distributions) before and after mercury entrapment suggests that the critical pore sizes guarding access to the majority of the mesopore network are at the lower end of the pore size distribution, suggesting connectivity is relatively low. This is consistent with the knee point in the conventional desorption isotherm occurring at a relative pressure lower than the onset of substantial capillary condensation on the adsorption branch. If it is assumed that pore lengths are proportional to the inverse square of diameter (or that pore number is proportional to incremental volume in the PSD), then the pore connectivity of the mesopore network (lower hysteresis zone) of H1, using the Mason (1982) method, is 2.8, which is very low and close to that (2) corresponding to just a corrugated through pore.

Further, it also noted that the width of the hysteresis of the superposed sorption isotherms from after entrapment has increased relative to that beforehand. This means that desorption of condensate in the sample with entrapped mercury is delayed to lower pressures than for before porosimetry. This may be because the empty macropores that previously would have provided nearby vapour phase seed sites for facilitating evaporation have become filled with entrapped mercury. This is indicated from the increase in hysteresis width found even following much lower levels of mercury entrapment, including where some of the smaller pores from the lower macropore mode are still left unfilled (as shown in the examples given in the Supplementary Material Figure S6).

A detailed comparison of gas sorption isotherm data before and after mercury entrapment, using incremental volume difference plots, can probe the spatial disposition of the different pore sizes and their relative accessibilities. The incremental amounts of nitrogen adsorbed in each relative pressure step following mercury intrusion to 5336 psia were subtracted from the corresponding amounts obtained before mercury entrapment. This means that if the same amount of adsorption was occurring at the same relative pressure both before and after mercury entrapment then the incremental difference would be close to zero (allowing for small amounts of random error). Whereas, if there was a decline, or increase, in amount adsorbed at a particular relative pressure following entrapment there would be either a positive, or negative, peak, respectively. The differences in incremental amount adsorbed as a function of relative pressure, thereby obtained for each sample H1-4, are shown in Fig. 9. The corresponding plots for the differences in incremental amount adsorbed as a function of pore size are included in the Supplementary Material (Figure S7). From Fig. 9, it can be seen that, for samples H1-3, as one moves from lower to higher pressures, the differences in adsorption between before and after mercury entrapment rise steeply to a sharp peak, which for H1 and H3 is markedly asymmetric with the steepest side towards lower pressures. The difference for sample H4 rises less sharply than for H1-3, but starts to rise significantly above the noise level at a relative pressure of ~ 0.949. Moving from low to high pressure, the tops of the initial cliff in the incremental difference plots occur at relative pressures of 0.939, 0.964, and 0.969 for samples H1, H2 and H3, respectively. Assuming adsorption according to a cylindrical sleeve meniscus, and using the Harkins-Jura equation for the t-layer correction, these peak relative pressures for H1, H2, and H3 correspond to pore diameters of 18.2, 29.3, and 33.7 nm, respectively (see Figure S7 in Supplementary Material). For condensation according to a hemispherical meniscus, a relative pressure of 0.939 for H1 would correspond to a pore diameter of 33.3 nm. It is noted that, from the Kloubek (1981) correlation, a mercury intrusion pressure of 5336 psia corresponds to a pore diameter of 32 nm.

The lack of any substantial negative peaks in the incremental difference plots in Fig. 9, and the similarities of the pore diameters corresponding to the lower pressure side sharp cut-off in the incremental difference plot, and the ultimate mercury intrusion pressure, suggests that mercury entrapment completely fills the pores in which it arises for samples H1-H4. This is because partial filling of pores with entrapped mercury would look like a loss of larger pores coupled with the apparent creation of new smaller pores, leading to the development of a substantial (i.e., of similar magnitude to positive peak) negative peak on the lower pressure side of the positive peak, which does not happen.

The incremental amounts of nitrogen adsorbed in each relative pressure step following mercury intrusion, to 1200 psia for samples H1-3 and 3800 psia for sample H4, were subtracted from the corresponding amounts obtained before mercury entrapment. The plots of these incremental differences against relative pressure are shown in Fig. 10. The corresponding plots for the differences in incremental amount adsorbed as a function of pore size are included in the Supplementary Material (Figure S8). It can be seen that the forms of the plots in Fig. 10 are more

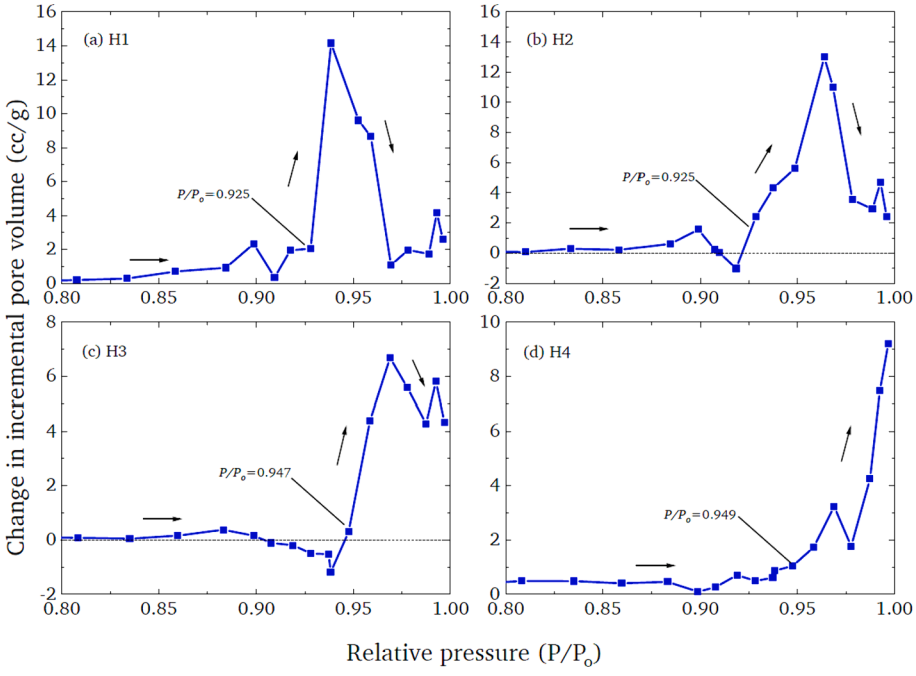

Fig. 9. Plots of the difference in incremental amount adsorbed between before and after mercury intrusion to 5336 psia, as a function of relative pressure for samples of H1(a), H2(b), H3(c), and H4(d).

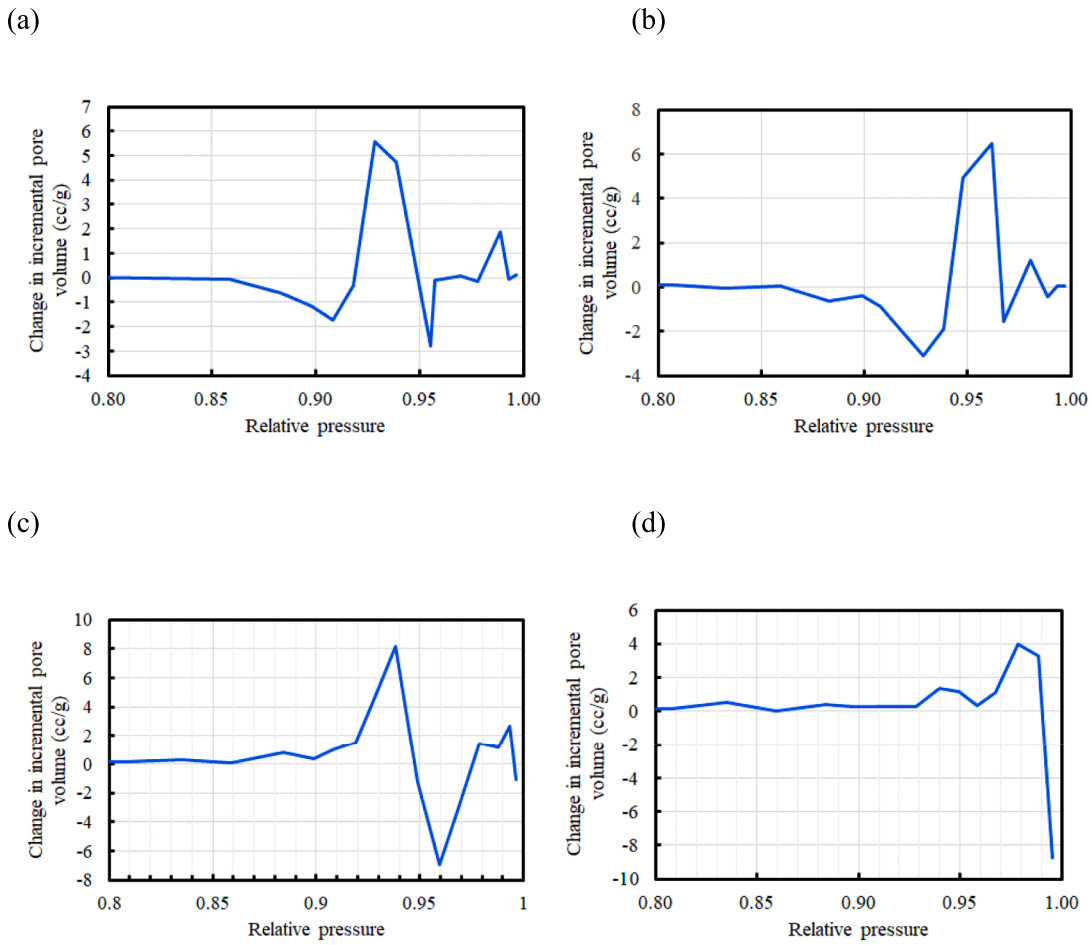

Fig. 10. Plots of the difference in incremental amount adsorbed between before and after mercury intrusion to 1200 psia, as a function of relative pressure, for samples of H1(a), H2(b), and H3(c), and before and after mercury intrusion to 3800 psia for sample H4(d).

complex than those shown in Fig. 9, especially as there are also now substantial negative peaks in the former. It is noted that, in critical pore size terms, a mercury intrusion pressure of 1200 psia or 3800 psia is equivalent to a nitrogen condensation pressure of 0.9867 or 0.9565, respectively, for a hemispherical meniscus, and 0.9933 or 0.9779, respectively, for a cylindrical sleeve meniscus. For samples H1 and H3 there are significant positive peaks at relative pressures of 0.9989, and 0.9875–0.9934, respectively. For sample H4, there are significant positive peaks at relative pressures of 0.9675–0.9889. These relative pressures exceed the critical cut-off values expected to correspond to pores that have become filled with entrapped mercury, and thus probably correspond to pores where access has been lost directly due to being filled with entrapped mercury.

However, in Fig. 10, there are also several positive and negative peaks for samples H1-4 for relative pressures below these cut-offs. These peaks represent changes in capillary condensation in still accessible porosity caused by the entrapment of mercury elsewhere. Once such scenario is where the entrapment of mercury in an immediate neighbouring pore transforms an unoccupied through pore into a dead-end pore. This would mean that the meniscus geometry for condensation may change from a cylindrical sleeve to a hemisphere, leading to a drop in the condensation pressure required to fill the pore. This would be manifested in the incremental difference plots as a positive peak where the previous cylindrical sleeve condensation occurred and a negative peak where the new hemispherical mode condensation occurred. The Cohan (1938) equation predicts that the locations of these peaks will be related such that the negative peak will occur at a relative pressure that is the square root of the relative pressure of the positive peak. For sample H1, a broad negative peak occurs over relative pressures of ~ 0.86–0.92, which corresponds to the square root of relative pressures ~ 0.93–0.96. It is noted that a large positive peak occurs in this range, though its area is much bigger than the negative peak. For sample H2, positive peaks occur at relative pressures of ~ 0.98, and ~ 0.962–0.947, while negative peaks occur at relative pressures of ~ 0.967 and 0.938–0.88. These relative pressures consist of two pairs of values for positive and negative peaks that match the predictions of the Cohan (1938) equations. For sample H3, there is a large negative peak at a relative pressure of 0.96, which is the square root of 0.98, that is the location of a smaller positive peak.

The impact of the mercury entrapment on nitrogen adsorption may lead to another effect that will overlap with the first effect discussed in the previous paragraph. It is possible that mercury entrapment in larger pores, of sizes above the critical intrusion size, may block access from the exterior (and thus to nitrogen) for pores smaller than the cut-off, even though these pores remain unintruded with mercury, but are completely surrounded by pores that are. In that case entrapped mercury will disconnect these pores from the remaining network. This effect would be manifested in the incremental difference plot by a positive peak below the critical relative pressure cut-off, but without an attendant negative peak at the square root value. For example, this occurs for sample H3, where there is a large positive peak for relative pressures in the range ~ 0.9–0.94, but no negative peak at all for pressures below this range. For samples H1 and H2, the observed positive peaks arising below the critical cut-off pressure are larger in size than the corresponding

negative peaks at the position corresponding to the square root of the pressure for the positive peak. This suggests that some of the contribution to the positive peak is also arising from the second effect described here. In contrast, the large negative deviation occurring at the extreme high end of pressure of the incremental plot for sample H4 may, by its location, be just due to the increased uncertainty in pressure values close to the saturation pressure for the apparatus used.

6. Rate of adsorption

Nitrogen gas kinetic uptake experiments were conducted for samples H1-4 at low pressure, and examples of typical raw data-sets are shown in the Supplementary Material (Figure S9). These data were fitted to the linear driving force (LDF) model to obtain the mass transfer coefficient, and examples of these fits are also shown in Figure S9. Fig. 11 shows comparisons of the ratio (k/k_0) of the adsorption-corrected LDF mass transfer coefficients for before and after blocking different volumes of void space with entrapped mercury for samples H1-4. Also shown in Fig. 11 is the prediction for the ratio of mass transfer coefficients expected from the Prager (1960) model described in the Theory section (Eq. (4). It can be seen that the experimentally measured ratios are all much lower than the Prager (1960) model predictions. The significant drop in the MTC for even a very small loss of pellet porosity observed for the HTS pellets is different to what has been observed previously (Mousa et al., 2023a) for fresh methanol synthesis pellets, where the drop in MTC was consistent with that expected for a random distribution of entrapped mercury at low levels.

Fig. 12 shows a plot of eq. (8) for the experimentally measured values of k/k_0 against $(1\text{-}s)^2$ with s taken from the values obtained with conventional gas sorption given in Table 2, and thus represents the saturation within the pellet feed particles only. From Fig. 12, it can be seen that these data have the form of a straight line, for the upper range of the abscissa variable (shown as circle symbols) down to the cut-off of ~ 0.47, as denoted by the vertical dashed line in Fig. 12. The data above this cutoff were fitted to eq. (8), and a statistically significant fit was

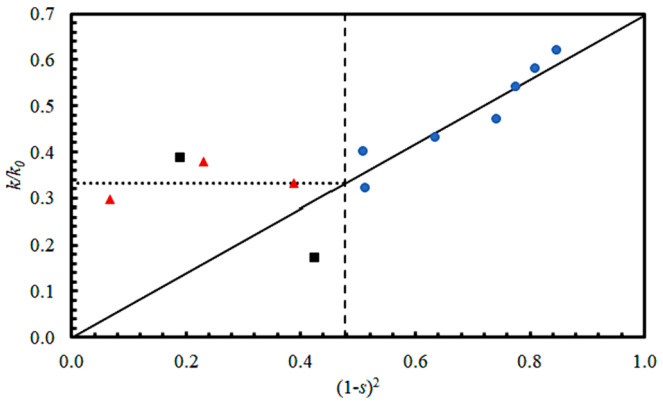

Fig. 12. Fit of experimental nitrogen gas uptake data to Eq. (8) (solid line), as described in main text, for partly mercury saturated samples listed in Table 2 (all samples with mercury saturation levels below (●), samples H1 and H2 with mercury saturation above (▲), and (■) sample H3 with mercury saturation above, the 3D percolation threshold). The vertical dashed line is for the value of s that corresponds to the percolation threshold for 3D site percolation on simple cubic lattice. The horizontal dotted line corresponds to the parameter calculated from Eq. (8) with the mercury saturation corresponding to the 3D percolation threshold (0.31).

obtained ($F = 1427$, $p = 2.5 \times 10^{-7}$), with an adjusted coefficient of determination of 0.83. This fitted straight line is also shown in Fig. 12, and has a gradient of 0.70 ± 0.04 (±95 % CI). From eq. (8), the linear form of the function fitted to the plot of k/k_0 against $(1\text{-}s)^2$ in Fig. 12 suggests that the ratio of critical pore sizes for the pellets before and after mercury entrapment is a constant equal to 0.70 ± 0.04 for the upper range in the abscissa variable.

It is noted that this gradient value (for the solid line in Fig. 12) is within experimental error of the ratio of volume-weighted average pore diameter after mercury intrusion to pressures ≥ 5336 psia to that

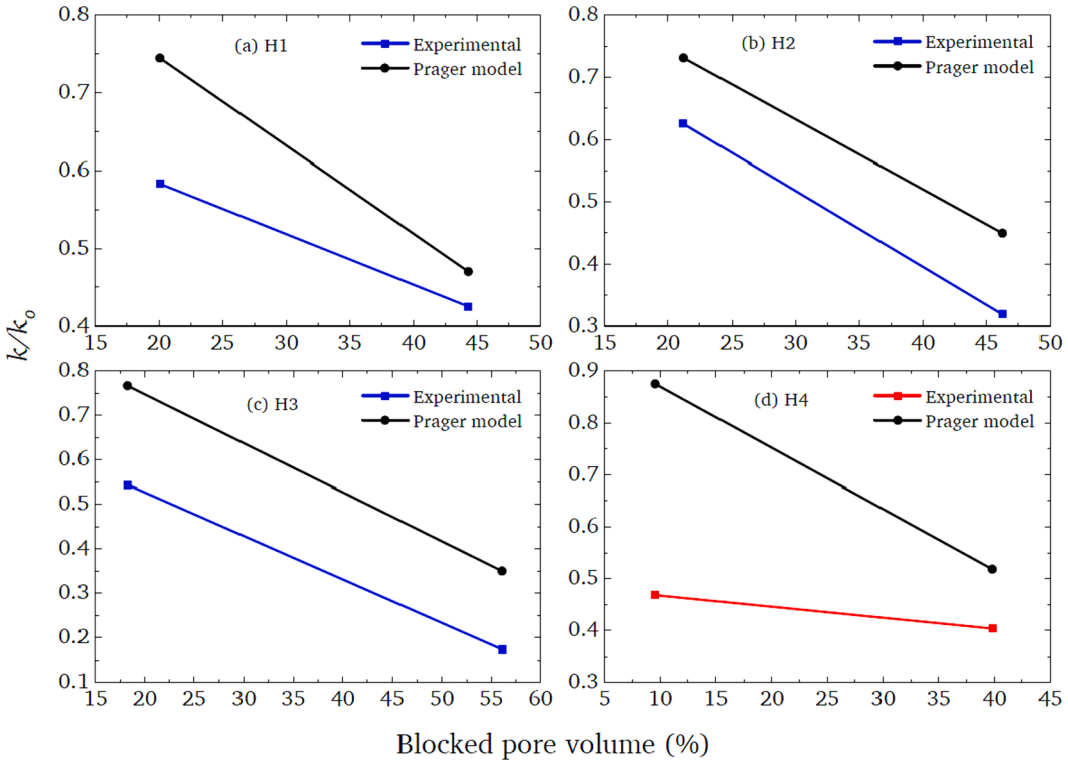

Fig. 11. Variation of the ratio of the mass transfer coefficient after mercury entrapment to that for an empty sample, with blocked pore volume, for samples of H1(a), H2(b), H3(c), and H4(d). Also shown is a comparison with the predictions of the Prager (1960) model.

beforehand for both samples H1 and H2, as given in Table 2. As can be seen from Figure S4, mercury intrusion to an ultimate pressure of 5336 psia, or greater, leads to the complete blocking of access of nitrogen to the pores in the upper zone of the hysteresis loop, leaving just the lower part empty. This finding of the similarity of the slope of the line in Fig. 12, and the aforementioned volume-weighted mean, suggests that, once mercury begins to become entrapped in the pore network, the critical pore size becomes the volume-weighted mean for the pores of the lower zone of the hysteresis loop.

The vertical dashed line in Fig. 12 indicates the value of $(1\text{-}s)^2$ that would correspond with the percolation threshold for the mercury saturated pores within the pellet feed particles. The percolation threshold for site percolation on a 3D cubic lattice (as is often used to house a random cluster model) is 0.31. It is noted that the percolation threshold is 0.29 for a three-dimensional isotropic Poisson polyhedral lattice (Larmier et al., 2016), which is similar. Hence, the values of fractional mercury saturation (or inaccessible void volume), as measured by conventional gas sorption, for the data-points with abscissa variable value below 0.47 in Fig. 12 have values (see Table 2) that exceed the percolation threshold. The location of the kink in the trend in the data in Fig. 12 is thus also consistent with a random cluster being a good model for the macroscopic structure of the pellets, as it occurs where might be expected for a RC structure, as will be explained below.

It is suggested that it is specifically the second mode of intermediate-sized macropores, which give rise to the upper zone of the conventional gas sorption isotherms, that form an incipiently percolating network of sites, embedded in a surrounding matrix containing the smaller mesopores, that is modelled by the random cluster model. It is thus the mercury saturation in the void space probed by conventional nitrogen sorption that is the characteristic parameter of the model, rather than the total mercury saturation including that in the very large macropores, seen in CXT images. Hence, it is the intermediate-sized macropores that would have an overall fraction of the whole void space enough to create a sample-spanning, percolating cluster. It is, perhaps, surprising that the very large macropores are not important to the model, but the over-condensation data suggests that these pores are mostly shielded by the smaller macropores of the intermediate-sized mode, and it these latter pores that control the mass transport, and, thence, their parameters that exhibit a discernable pattern, as seen in Fig. 12, commensurate with a random cluster representation.

The suggestion of the presence of an incipiently percolating cluster of the intermediate-sized macropores in the empty samples is also consistent with various other aspects of the data given above. The general lack of a significant shift in the upper half of the low pressure mercury intrusion mode for fragmented samples compared with whole pellets (seen in Figure S3) suggests that (virtually) all the intermediate-sized macropores are already generally accessible from the exterior for the whole pellets or from intruded very large macropores, and, thence, form part of a percolating network. This is also consistent with the observation above that hysteresis width, for the upper, higher relative pressure region of the sorption isotherms for samples H1-H3, (in Fig. 7) is, apparently, of solely single pore origin. An incipiently percolating cluster, with, consequently, relatively few branches from the critical path, is very similar to the 1D corrugated array of cylindrical pore segments proposed by Valiullin and co-workers to study advanced condensation (Enninful et al., 2021).

The presence of an incipiently percolating network of the second mode, intermediate-sized macropores is also consistent with the substantial drop in measured mass transfer coefficient below that expected for a random arrangement of entrapped mercury, seen in Fig. 11, even for relatively very low amounts of entrapped mercury, and also the observed slope of the solid line fit in Fig. 12. This is because, if the intermediate-sized macropore network, is incipiently percolating, then just a small loss of pores in the network would stop it percolating and acting as a fast conduit for mass transfer. Instead, at some point in the macropore network, the blockage with entrapped mercury would mean that the diffusive flux was forced to deviate around via an alternate pathway necessarily through the empty mesoporous regions. Since critical path theory suggests that the rate of mass transport is controlled by the largest resistance in the flow path (Ambegaokar et al., 1971), then this is consistent with the ratio of the critical pore sizes (from slope of solid line in Fig. 12 and eq. (8)) corresponding to the (predominant) ratio of the volume-weighted means of the pore size distributions from before and after entrapment blocking the intermediate macropores (from Table 2).

If the individual intermediate-sized (second mode) macropores forming the percolating cluster were pervasively embedded within a connecting mesoporous matrix then there would not be expected to be any prevention of condensation within the macropores due to mercury entrapment. This is because the mesopores, being smaller, would fill up with condensate at lower relative pressures, and present free menisci at the boundaries of the still vapour-filled larger macropores. The larger macropores could then fill with condensate, supplied via these connecting mesopores, when the relevant critical vapour pressure was reached. However, the incremental difference plots, for samples with the larger macropore network partially-saturated with entrapped mercury (Fig. 10), suggest that some macropores are, in fact, isolated from the whole of the rest of the void space by the mercury entrapment, since they do not fill with nitrogen at all. Since no mercury has entered the mesopores during the mercury porosimetry scanning curve experiments in question, and so the mesopores would still be empty, this means that the larger macropores that become isolated cannot be, in fact, embedded within a mesoporous matrix after all. This suggests that there must be some spatial segregation between the pores in the mesopore and macropore modes of the mercury intrusion curve. This proposed spatial segregation is consistent with the observation from the CXT images (in Figs. 2-5) of samples following partial mercury intrusion of the macropore mode that there is a distinctive patchwork of empty black and mercury-filled white feed particles across the pellet, rather than a more homogeneous distribution of entrapped mercury. Further, for the example CXT image shown in Figure S1(b), it was seen that the distribution of pixel intensities is bimodal, with two clear peaks corresponding to the mercury-containing and empty image pixels, suggesting a relative segregation of mercury-penetrated and more empty regions at this stage in the intrusion. This observation is also consistent with the mercury saturation also being viewed as the volume fraction of pellet considered belonging to the RC. Hence, the percolating cluster of intermediate-sized macropores must consist of a pathway formed from progressively moving from one feed particle containing larger macropores to an immediately adjacent similar feed particle, rather like stepping stones across a pond. However, when a critical one of these ‘stepping stones’ is removed via mercury entrapment, the pathway must enter the surrounding ‘pond’ of feed particles containing only mesopores. This is reflected in the drop in the critical pore size then controlling diffusion, as measured by the slope of the solid line in Fig. 12, thereby reducing mass transport rates drastically, as seen in Fig. 11. The loss of access to some mesoporosity due to mercury entrapment in macropores seen in Fig. 8(b) is also consistent with the intermediate-sized macroporosity being vital access routes to smaller pores. The filling of the intermediate-sized macropores (second mode) and larger mesopores eventually cut off and isolated some mesopores, maybe in a manner as suggested by the dark patches surrounded by bright white patches evident in Figs. 2-5.

It was noted above that the data in Fig. 12 with abscissa variable values below ~ 0.47 did not follow the main trend for the other data in the upper range shown by the fitted solid line, but appear to plateau out (with an average value of k/k_0 of 0.336), as indicated by the horizontal dotted line in Fig. 12. The data in the lower range correspond to experiments whereby mercury entrapment affects accessibility of the lower zone of the hysteresis loop (that occurs for samples H1-3). While the other data-point for H3 is consistent with that for H1 and H2, it is noted that the point for H3 following intrusion to 5336 psia to the left of

the vertical dashed line value of k/k_0 lies well below that expected from either the solid line or dotted line. However, if allowance is made for the lower volume-weighted mean pore size of the remaining accessible pore volume for this point, as shown in Table 2, suggesting that the critical pore size may be reduced, then the predicted value of k/k_0 is then 0.23, which is much closer to the experimental measurement.

The aforementioned tendency for the value of k/k_0 to plateau below a value of $(1\text{-}s)^2$ of 0.47 may be due to a change in the pattern of mercury entrapment once the mercury saturation exceeds the percolation threshold. The value of k/k_0 at this particular point would be given by Eq. (8) where the mercury saturation within feed particles corresponds to the critical value of the percolation threshold in 3D (of 0.31), and r/r_0 corresponds to that of the matrix (~0.7), and is shown in Fig. 12 by the horizontal dotted line. It can also be seen from Fig. 12 that the experimental data does, indeed, plateau around this value. At the percolation threshold, mercury can penetrate all the way to the centre of the pellet, and entrapment can accumulate there, like the metallic core of a planet, as shown in Fig. 13. A similar scenario has been observed previously for mercury entrapment in some fresh and some aged (from use on-stream) methanol synthesis catalyst pellets (Nepryahin et al., 2016; Mousa et al., 2023b). If such a scenario occurred, then the 'core' of entrapped mercury could expand more, or less, isotropically in all directions if the sample is approximately homogeneous over the largest length-scales (larger than the feed particle sizes, and of the scale of the pellet itself). Hence, the height of the mercury core ($2\,h$ in Fig. 13) is likely to grow linearly with mercury saturation (equal to one minus porosity). It is also noted that the pellets have a larger diameter (~7 mm) than height (~4 mm), as shown in Table 1 and Fig. 13. Hence, the characteristic diffusion penetration depth a is likely to be the half-height (as shown in Fig. 13), as this is the shortest straight-line penetration path for the mass transfer flux. This penetration depth will decline linearly as the height of the mercury core expands, as entrapped mercury saturation increases. Therefore, if the tortuosity of the remaining accessible pore network is given by Eq. (5), then, from Equation (3) and Equation (6), it would be expected that:

$$\frac{k}{k_0} = \frac{\varepsilon^2}{\varepsilon_0^2}\frac{a_0^2}{a^2} = \left(1 - s^2\right)\frac{a_0^2}{a^2} = constant \tag{9}$$

and, thence, ε/a = constant, because a will also decline linearly to compensate as the remaining accessible porosity ε declines. Hence, the scenario shown in Fig. 13 is consistent with the form of the mass transport data in Fig. 12. However, in this case, it was not possible to examine the mercury spatial distribution in the pellets at high saturations because the X-rays were unable to penetrate the sample when full of so much mercury, as it is so electron-dense and absorbs X-rays strongly. The scatter of the data points for high saturation about the horizontal dotted line in Fig. 12 may be due to some slight variation from homogeneity at larger length-scales.

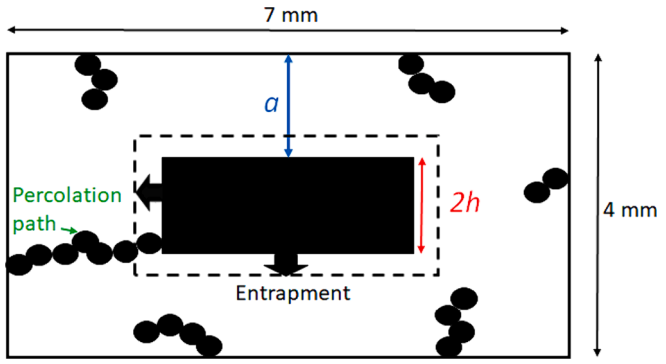

Fig. 13. Schematic diagram of a diametric cross-section through a pellet depicting the scenario proposed in the main text for the pattern of mercury entrapment once the mercury saturation exceeds the percolation threshold. The central black rectangle, of height $2\,h$, represents the mercury entrapped in the pellet core, while the black ovals represent mercury entrapped in feed particles in the surrounding 'mantle'. The broad arrows indicate the directions of expansion of the core, to a position shown by dashed rectangle, as mercury entrapment increases.

It was found that, despite their differences in porosity and surface area given in Table 1, the RC model was found to suitable for all three samples H1-3. In contrast, it is noted that the minimalist idealization, namely a random pore bond network, needed for modelling the cylindrical methanol synthesis pellets studied in previous work is different to that needed for HTS pellets even though one batch of the methanol synthesis pellets studied was also made using roll-compacted feed (Mousa et al., 2023a,b). This difference in the morphology of the structural model needed for the two different types of catalyst pellet arises from differences in the critical aspect of the pore structure identified as controlling mass transport in each case. For the fresh methanol synthesis pellets, mass transport was controlled by surface clusters of large pores. The difference in the spatial distribution of pellet density and pore size between methanol and HTS pellets may have been caused by a different stress distribution during tableting, which may have arisen from the different pellet shapes and feed materials, and will be the subject of future work.

7. Conclusions

This work has shown that the rarely-used, gas overcondensation method can reveal the full hierarchy in the pellet structure not immediately apparent from other data. The differential analysis of integrated gas sorption data obtained before and after mercury entrapment has provided a detailed and statistically-representative assessment of the accessibility of particular pore size bins not so easily obtained from imaging.

It has been found that a minimalist idealization modelling strategy can successfully explain the variation in mass transport properties due to progressive modification of the pore structure of the HTS catalyst pellets. It has been found that a random cluster model for the spatial distribution of entrapped mercury can account for the variation in gas phase mass transport in the remainder of the void space following the progressive filling of the macropore network with mercury. The CXT image data suggested that this may be because the feed particles had a broad distribution of densities (and pore sizes) that are spatially distributed at random through the die during filling in the tableting process. The pellets contained an incipiently percolating network of intermediate-sized macropores that formed the second of a trimodal pore size distribution, and was critical to mass transport, as shown by the dramatic drop in rates when just part of it was lost to entrapped mercury. These critical macropores provide a 'super highway' to the central core region of the pellet making it highly accessible for mass transport, as shown by the likely accumulation of entrapped mercury there, once the percolation threshold was exceeded.

The comparison of the findings described here for HTS pellets, with those from previous work for methanol synthesis catalysts, shows how even superficially similar pellets (both made by tableting of roll-compacted feed particles) can have very different fundamental structure-transport relationships. This exemplifies why the 'filtering' or 'sifting' strategy described above is required on a case-by-case basis to determine the critical aspects of a given pore structure that control mass transport.

CRediT authorship contribution statement

Suleiman Mousa: Writing – original draft, Methodology, Investigation, Conceptualization. **Toby Beech:** Methodology, Investigation. **Emma Softley:** Writing – original draft, Methodology, Investigation. **Robin S. Fletcher:** Writing – review & editing, Writing – original draft, Resources, Methodology, Investigation, Conceptualization. **Gordon**

Kelly: Writing – original draft, Supervision, Resources, Project administration, Funding acquisition. **Emily Viney:** Writing – original draft, Supervision, Resources, Project administration, Funding acquisition. **Sean P. Rigby:** .

Declaration of competing interest

The authors declare that they have no known competing financial interests or personal relationships that could have appeared to influence the work reported in this paper.

Data availability

The data that has been used is confidential.

Acknowledgements

This work was supported by the Engineering and Physical Sciences Research Council [grant number EP/R512059/1]. We thank Martin Corfield for help with producing the CXT images.

Appendix A. Supplementary data

Supplementary data to this article can be found online at https://doi.org/10.1016/j.ces.2024.120005.

References

Almazán-Almazán, M.C., López-Domingo, F.J., Domingo-García, M., Léonard, A., Pérez-Mendoza, M., Pirard, J.P., López-Garzón, F.J., Blacher, S., 2011. Influence of carbon xerogel textural properties on the dynamic adsorption of methyl iodide. Chem. Eng. J. 173, 19–28.

Ambegaokar, V., Halperin, B.I., Langer, J.S., 1971. Hopping conductivity in disordered systems. Phys. Rev. B 4, 2615–2620.

Bare, S.R., Charochak, M.E., Kelly, S.D., Lai, B., Wang, J., Chen-Wiegart, Y.K., 2014. Characterization of a fluidized catalytic cracking catalyst on ensemble and individual particle level by X-ray micro- and nanotomography, micro-X-ray fluorescence and micro X-ray diffraction. Chem. Cat. Chem. 6, 1427–1437.

Barrett, E.P., Joyner, L.G., Halenda, P.P., 1951. The determination of pore volume and area distributions in porous substances. I. Computations from nitrogen isotherms. J. Am. Chem. Soc. 73, 373–380.

Chen, F., Mourhatch, R., Tsotsis, T.T., Sahimi, M., 2008. Pore network model of transport and separation of binary gas mixtures in nanoporous membranes. J. Membr. Sci. 315, 48–57.

Cody, G.D., Davis, A., 1991. Direct imaging of coal pore space accessible to liquid metal. Energy Fuel 5 (6), 776–781.

Cohan, L.H., 1938. Sorption hysteresis and the vapor pressure of concave surfaces. J. Am. Chem. Soc. 60, 433–435.

Crank, J., 1975. The mathematics of diffusion, 2nd ed. Clarendon Press, Oxford.

Dudhat, S.M., Kettler, C.N., Dave, R.H., 2017. To study capping or lamination tendency of tablets through evaluation of powder rheological properties and tablet mechanical properties of directly compressible blends. AAPS Pharm. Sci. Tech. 18, 1177–1189.

Elias-Kohav, T., Sheintuch, M., Avnir, D., 1991. Steady-state diffusion and reactions in catalytic fractal porous media. Chem. Eng. Sci. 46, 2787–2798.

Elsergany, R.N., Chan, L.W., Heng, P.W.S., 2020. Cushioning pellets based on microcrystalline cellulose – crospovidone blends for MUPS tableting. Int. J. Pharm. 586, 119573.

Enninful, H.R.N.B., Schneider, D., Rudolph, B., Meyer, A., Mascotto, S., Valiullin, R., 2021. Nuclear magnetic resonance cryoporometry study of solid-liquid equilibria in interconnected spherical nanocages. J. Phys. Chem. C 125, 26916.

Fusi, N., Martinez-Martinez, J., 2013. Mercury porosimetry as a tool for improving quality of micro-CT images in low porosity carbonate rocks. Eng. Geol. 166, 272–282.

Hill-Casey, F., Hotchkiss, T., Hardstone, K.A., Hitchcock, I., Novak, V., Schlepütz, C.M., Meersmann, T., Pavlovskaya, G.E., Rigby, S.P., 2021. Hyperpolarised xenon MRI and time-resolved X-ray computed tomography studies of structure-transport relationships in hierarchical porous media. Chem. Eng. J. 405, 126750.

Hitchcock, I., Lunel, M., Bakalis, S., Fletcher, R.S., Holt, E.M., Rigby, S.P., 2014. Improving sensitivity and accuracy of pore structural characterisation using scanning curves in integrated gas sorption and mercury porosimetry experiments. J. Colloid Interface Sci. 417, 88–99.

Hollewand, M.P., Gladden, L.F., 1992. Modelling of diffusion and reaction in porous catalysts using a random three-dimensional network model. Chem Eng Sci 47, 1761–1770.

Jacobsen, H.S., Puig-Molina, A., Dalskov, N., Frandsen, H.L., 2016. 3D mapping of density and crack propagation through sintering of catalyst tablets by X-ray tomography. Advances in Ceramic Armor, Bioceramics, and Porous Materials 163–170.

Kloubek, J., 1981. Hysteresis in porosimetry. Powder Technol. 29 (1981), 63–73.

Kolitcheff, S., Jolimaitre, E., Hugon, A., Verstraete, J., Carrette, P.-L., Tayakout-Fayolle, M., 2017. Tortuosity of mesoporous alumina catalyst supports: influence of the pore network organization. Microporous Mesoporous Mater. 248, 91–98.

Larmier, C., Dumonteil, E., Malvagi, F., Mazzolo, A., Zoia, A., 2016. Finite-size effects and percolation properties of poisson geometries. Phys. Rev. E 012130.

Makovetsky, R., Piche, N., March, M., 2018. Dragonfly as a platform for easy image based deep learning applications. Microsc. Microanal. 24, 532–533.

Mousa, S., Novak, V., Fletcher, R.S., Garcia, M., Mcleod, N., Corfield, M., Rigby, S.P., 2023a. Integration of multi-scale porosimetry and multi-modal imaging in the study of structure-transport relationships in porous catalyst pellets. Chem. Eng. J. 452, 139122.

Mousa, S., Novak, V., Fletcher, R.S., Kelly, G., Garcia, M., Mcleod, N., Parmenter, C., Rigby, S.P., 2023b. Evolution of the pore structure-transport relationship during catalyst reduction and sintering studied by integrated multi-scale porosimetry and multi-modal imaging. Chem. Eng. Sci. 277, 118880.

Murray, K.L., Seaton, N.A., Day, M.A., 1999. An adsorption-based method for the characterization of pore networks containing both mesopores and macropores. Langmuir 15, 6728–6737.

Neimark, A.V., Ravikovitch, P.I., 2001. Capillary condensation in MMS and pore structure characterization. Micropor Mesopor Mater. 44, 697–707.

Nepryahin, A., Fletcher, R.S., Holt, E.M., Rigby, S.P., 2016. Structure-transport relationships in disordered solids using integrated rate of gas sorption and mercury porosimetry. Chem Eng Sci 152, 663–673.

Pavlovskaya, G.E., Meersmann, T., Jin, C., Rigby, S.P., 2018. Fluid flow in a porous medium with transverse permeability discontinuity. Phys. Rev. Fluids 3, 044102.

Pini, R., Joss, L., Hejazi, S.A.H., 2021. Quantitative imaging of gas adsorption equilibrium and dynamics by X-ray computed tomography. Adsorption 27, 801–818.

Prager, S., 1960. Diffusion in inhomogeneous media. J. Chem. Phys. 33, 122–127.

Qi, Y., Liu, K., Peng, Y., Wang, J., Zhou, C., Yan, D., Zeng, Q., 2021. Visualization of mercury percolation in porous hardened cement paste by means of X-ray computed tomography. Cem. Concr. Compos. 122, 104111.

Qian, R., Zhang, Y., Liu, C., Yang, L., Liu, G., She, W., 2018. Quantitative characterization of three-dimensional pore structure in hardened cement paste using X-ray microtomography combined with centrifuge driven metal alloy intrusion. Mater Charact 145, 277–283.

Raeini, A.Q., Bijeljic, B., Blunt, M.J., 2017. Generalized network modeling: network extraction as a coarse-scale discretization of the void space of porous media. Phys. Rev. E 96, 013312.

Rieckmann, C., Keil, F.J., 1999. Simulation and experiment of multicomponent diffusion and reaction in three-dimensional networks. Chem. Eng. Sci. 54, 3485–3493.

Rigby, S.P., 2020. Structural characterisation of natural and industrial porous materials: a manual. Springer International Publishing, Cham.

Rigby, S.P., 2023. The anatomy of amorphous. Heterogeneous Catalyst Pellets. Materials 16, 3205.

Rigby, S.P., Gladden, L.F., 1996. NMR and fractal modelling studies of transport in porous media. Chem. Eng. Sci. 51, 2263–2272.

Rigby, S.P., Fletcher, R.S., Riley, S.N., 2004. Characterisation of porous solids using integrated nitrogen sorption and mercury porosimetry. Chem. Eng. Sci. 59, 41–51.

Ronneberger, O., Fischer, P., Brox, T., 2015. U-net: convolutional networks for biomedical image segmentation. International Conference on Medical Image 9351, 234–241.

Ruffino, L., Mann, R., Oldman, R., Stitt, E.H., Boller, E., Cloetens, P., DiMichiel, M., Merino, J., 2005. Using x-ray microtomography for characterisation of catalyst particle pore structure. Can J Chem Eng 83, 132–139.

Seaton, N.A., 1991. Determination of the connectivity of porous solids from nitrogen sorption measurements. Chem Eng Sci 46, 1895–1909.

Seely, R., Liddy, T.J., Rochelle, C.A., Fletcher, R.S., Rigby, S.P., 2022. Evolution of the mineralogy, pore structure and transport properties of Nordland Shale following exposure to supercritical carbon dioxide. J. Pet. Sci. Eng. 213, 110466.

Twigg, M.V. (2014). The Catalyst Handbook, second ed. CRC Press, Taylor & Francis Group, Boca Raton, FL.

Wakao, N., Smith, J.N., 1962. Diffusion in catalyst pellets. Chem. Eng. Sci. 17, 825–834.

Walker, W.J., Reed, J.S., Verma, S.K., 1999. Influence of slurry parameters on the characteristics of spray-dried granules. J. Am. Ceram. Soc. 82, 1711–1719.

Weisberg, M., 2013. Simulation and similarity: using models to understand the world. Oxford University Press, Oxford, UK.

Zeiler, M.D., 2012. Adadelta: an adaptive learning rate method. Computing Research Repository 121 arXiv:1212.5701.

Zeng, Q., Chen, S., Pengcheng, Y., Peng, Y., Wang, J., Zhou, C., Wang, Z., Yan, D., 2020. Reassessment of mercury intrusion porosimetry for characterizing the pore structure of cement-based porous materials by monitoring the mercury entrapments with X-ray computed tomography. Cem. Concr. Compos. 113, 103726.